communications biology

A Nature Portfolio journal

Article

https://doi.org/10.1038/s42003-025-08003-0

Dynamic conformations of the P. furiosus MR-DNA complex link Mre11 nuclease activity to DNA-stimulated Rad50 ATP hydrolysis

Marella D. Canny[1,4], Mahtab Beikzadeh[2,4], Navneet Kaur[2,3], Rohan Pendse[2] & Michael P. Latham[1,2]

The MRE11-RAD50-NBS1/Xrs2 (MRN/X) protein complex has essential roles in the repair of damaged DNA. The current understanding of the conformational landscape of the core MR complex comes from various structural studies. However, given the heterogeneous nature of these structures, we suspect that several conformational states may still be unaccounted for. Here, we use methyl-based NMR experiments on *P. furiosus* MR to determine an ensemble of distinct conformations of MR bound to DNA, consistent with the highly dynamic nature of the MR-DNA complex. Interrogation of these structures via in vitro activity assays on MR mutants reveal an unexpected, striking correlation between the nuclease activity of Mre11 and the magnitude of DNA-stimulated ATP hydrolysis by Rad50. Together, the structures and activity data support a model for MR activity where DNA-stimulated ATP hydrolysis unlocks Rad50 to provide access to the Mre11 active sites and further demonstrate how a heterogeneous ensemble of conformations can be used to coordinate various functions to direct biological outcomes. By elucidating the dynamic conformations of the DNA-bound MR complex, this work lays the foundation for future studies aimed at further characterizing this landscape and dissecting its role in the molecular mechanism of DNA repair and genome stability.

DNA double-strand breaks (DSBs) to our genome are caused by exogenous factors such as ionizing radiation and radiomimetic drugs. More commonly, they result from endogenous processes such as abortive topoisomerase reactions, hairpin cleavage, and replication fork collapse arising from the collision of the replication and transcription machinery or replication over other forms of damaged DNA (e.g., single-strand breaks and cross-links)[1]. There are two major pathways for repairing DNA DSBs: nonhomologous end joining (NHEJ) and homologous recombination (HR)[2–4]. Central to each of these repair mechanisms and therefore the overall maintenance of genomic stability is the essential Mre11-Rad50 (MR) complex in bacteria/archaea and Mre11-Rad50-Nbs1/Xrs2 (MRN/X) complex in eukarya[5–7]. Through its multitude of activities, and in conjunction with other DNA damage repair proteins, MRN identifies broken DNA and initiates the repair processes.

The universally conserved core MR complex is composed of two Mre11 and two Rad50 subunits (i.e., M_2R_2, simply referred to as MR). Dimeric Mre11 is a Mn^{2+}-dependent nuclease with 3'-to-5' exonuclease activity[8,9] and endonuclease activity against a variety of DNA substrates, including protein-DNA adducts[10–12], DNA hairpins[13], and single-stranded DNA[8,9]. Bound to each Mre11 protomer is a Rad50, which is a member of the ATP-binding cassette (ABC) superfamily of ATPases[14]. The N- and C-terminal sub-domains of the ABC ATPase nucleotide-binding domain (NBD) are separated by 400–800 Å anti-parallel coiled-coils and an apical Zn^{2+} hook domain, which serves as a motif for Rad50 association[15]. ATP binding to each of the Rad50 NBDs activates the ATM/Tel1 protein kinase[16–19] in eukarya and subsequent hydrolysis of ATP modulates Mre11 nuclease activity[16,20–22]. Associated with each MR complex in eukarya is an Nbs1 (Xrs2 in *S. cerevisiae*), which is a flexible scaffolding protein that also

[1]Department of Biochemistry, Molecular Biology, and Biophysics, University of Minnesota, Minneapolis, MN, USA. [2]Department of Chemistry and Biochemistry, Texas Tech University, Lubbock, TX, USA. [3]Present address: Doherty Institute of Infection and Immunity, The University of Melbourne, Melbourne, Australia. [4]These authors contributed equally: Marella D. Canny, Mahtab Beikzadeh. e-mail: latha070@umn.edu

alters MR activity and helps to recruit downstream effectors to the site of the DNA DSB[23–27].

The entire toolbox of structural biology techniques has been applied to the MRN/X complex to understand the relationships between the structure and function of Mre11 and Rad50. There are numerous X-ray crystal structures of isolated Mre11 nuclease and capping domain ($Mre11^{ND}$)[28–31], isolated Rad50 nucleotide-binding domain ($Rad50^{NBD}$)[14,32], and MR^{NBD} complex in various states (Supplementary Fig. S1)[20,32–37]. More recently, cryo-electron microscopy (cryo-EM) has been utilized to determine structures of full-length MR bound to ATP, ADP and dsDNA, ADP and Ku-blocked dsDNA, or ADP and hairpin DNA structures (Supplementary Fig. S1)[38–40]. From these structures, several similarities and differences emerge. For example, all structures of nucleotide-bound Rad50 reveal the same 'closed' conformation, and in the context of the MR complex, the ATP-bound closed Rad50 occludes the Mre11 active sites[20,33,35,36,38]. Additionally, these structures clearly demonstrate that both Mre11 and the 'closed' conformation of Rad50 are capable of binding DNA (Supplementary Fig. S1). However, further comparison of these structures reveals both symmetrical and asymmetrical interactions between the DNA and protein. Dramatic asymmetries have been noted in cryo-EM structures where Rad50 interacts asymmetrically with respect to the Mre11 dimer to asymmetrically position a DNA substrate into one of the Mre11 active sites[38,39]. One interpretation for the observed conformational heterogeneity amongst all these structures is that the MR complex utilizes a variety of binding modes to recognize the myriad of substrates that occur upon a DNA DSB. Although it is tempting to view these structures as well-defined, static waypoints along the conformational path for MR, nuclease and ATPase activity assays, small angle X-ray scattering (SAXS) and luminescence resonance energy transfer (LRET) data have clearly shown that an ensemble of conformations exists in solution[16,32,41–43]. In fact, we previously combined LRET data with rigid body docking to propose three conformations of the *P. furiosus* (*Pf*) ATP-bound MR complex in solution: 'closed', 'partially open', and 'open'[43]. Mutagenesis studies determined that all three MR conformations play a role in the function of the complex. Critically, the LRET data indicate that these three states persist, though in different populations, without ATP as well as in the presence of DNA substrates[42,43].

Here, using side-chain methyl group-based NMR data and rigid-body docking, we investigated how the 200 kDa MR complex binds to a dsDNA DSB mimic in solution. NMR experiments were performed in the absence of ATP, since at least three conformations of the MR complex are all present in that condition[42,43] and an apo form of Rad50 is naturally part of its catalytic cycle. In fact, a closed conformation was observed for the cryo-EM model of *C. thermophilum* MR in the presence of ATPγS where only one of two ATP binding sites was occupied and the bound ATPγS was not making the canonical contacts with the Rad50 active site[40]. Furthermore, as the closed MR-DNA structure is well established, omitting ATP favors the conformational equilibrium in solution towards the partially open and open MR conformations, for which there are no existing high-resolution DNA-bound structures. Finally, it has been demonstrated that scanning for DNA DSBs and tethering those breaks occurs in the presence or absence of ATP[16,44,45], and activation of ATM/Tel1 starts from the apo form of the complex[19,46]. Thus, characterizing structures for the entire catalytic cycle of the MR complex (i.e., ATP-free, ATP-bound, ADP-bound) is critical to understanding how it functions in DNA DSB repair. To this end, NMR chemical shift perturbations (CSPs) and paramagnetic relaxation enhancements (PREs)-based distance restraints from dsDNA-bound MR complex were used in rigid-body docking calculations to determine models of dsDNA bound to each of the three *Pf* MR conformations. Importantly, an array of DNA-bound conformations is necessary to fully describe our NMR data, which underscores the heterogeneous and dynamic nature of the MR complex. To validate these structures, residues involved in MR-DNA interactions were mutated and the effects on DNA binding, nuclease activity, and ATP hydrolysis were interrogated. The functional data revealed a striking correlation between Mre11 nuclease activity and the allosteric stimulation of Rad50 ATP hydrolysis by a DNA DSB, which supports a model for the interplay of MR catalytic activities and suggests how scanning, DNA DSB recognition, and MR nuclease activities are coordinated.

Results

Multiple dsDNA-bound conformations of the MR^{NBD} complex in solution

NMR studies were performed on *Pf* Mre11 in complex with a commonly studied, truncated construct of *Pf* Rad50 that forms a functional NBD but does not contain the ~600–800 Å coiled-coil and Zn hook domains ($Rad50^{NBD}$)[14,16,32,47]. Our previous LRET studies have demonstrated that both the truncated and full-length *Pf* MR complex populate the same three conformations in solution and that substrate (i.e., ATP and/or DNA) binding affects both constructs in a similar manner[43]. Uniformly deuterated, side-chain methyl group $^{13}CH_3$-labeled (ILVM) samples of Mre11 and $Rad50^{NBD}$ were separately expressed and purified. MR^{NBD} complexes for NMR were made by mixing either ILVM-labeled Mre11 with unlabeled $Rad50^{NBD}$ or ILVM-labeled $Rad50^{NBD}$ with unlabeled Mre11. To determine the effects of DNA binding to the MR^{NBD} complex, a 15 base-pair hairpin DNA with a four-nucleotide loop and two nucleotide 3'-overhang, representing a broken dsDNA exonuclease and/or hairpin endonuclease substrate, was added to each sample.

NMR-observed DNA titration experiments were performed with the two labeled MR^{NBD} complexes. Both Mre11- and Rad50-ILVM labeled MR^{NBD} complexes revealed a single set of methyl group peaks upon the addition of the hairpin DNA consistent with an overall symmetrical complex (Figs. 1 and 2). The CSPs that occur to both Mre11 and $Rad50^{NBD}$ upon DNA binding are relatively small (Supplementary Data 1). When looking at the complex more closely, the reason becomes clear – there are very few solvent-exposed side-chain methyl groups that can make direct interactions with the DNA. Most of the interactions between MR and the DNA likely occur between polar residues that are above the buried ILVM residues. Thus, the majority of the CSPs are probably due to small changes in the chemical environment for a secondary shell of residues beneath the primary DNA binding residues. Moreover, small but meaningful side-chain methyl group CSPs have been noted in numerous systems including, but not limited to, chaperones, kinases, the proteasome, ubiquitin ligases, various enzymes, and the nucleosome (see ref. 48).

For Mre11, CSPs were observed across the top of the nuclease domain (e.g., L61 and M146) and the core of the capping domain (e.g., L314) (Fig. 1A). CSPs for residues in the nuclease domain were expected based on the previously reported X-ray crystal structure of $Mre11^{ND}$ bound to DNA substrates[29,30] and were similar to previously reported CSPs for the same DNA substrate binding to ILVM-labeled $Mre11^{ND}$ (ref. 49). For the titration of hairpin DNA into Mre11-labeled MR^{NBD} complex, the majority of the side-chain methyl group peaks were in fast exchange on the chemical shift timescale (Fig. 1A). Individually fitting these data to a simple two-state binding equation (Fig. 1B; Supplementary Data 2) gave a median apparent K_D ~ 5.4 μM (average K_D ~ 7.1 μM) consistent with the K_D value for DNA binding to ATP-free *Pf* MR^{NBD} complex at 50 °C[43]. Plotting the $\log_{10}(K_D)$ onto the methyl groups of $Mre11^{ND}$ (Fig. 1B) again shows the effect of DNA binding to the top of the Mre11 nuclease domain, around the active site, and throughout the capping domain.

For the $Rad50^{NBD}$-labeled MR^{NBD} complex, CSPs were observed on the 'top' (e.g., L51, L89, I97) and the 'bottom' (e.g., I837, L871, V881) of the NBD as well as in the coiled-coil region (I730) (Fig. 2A). As the NMR data are the result of the populated weighted average of all possible conformations of MR^{NBD} in solution, the multiple binding interfaces on Rad50 suggest the presence of at least two DNA-bound forms of *Pf* MR^{NBD} in solution. We assumed that the residues with CSPs on top of the Rad50 NBD correspond to a DNA binding surface in a closed conformation, which was previously demonstrated to be populated in apo MR^{NBD}[40,42,43]. Conversely, in the partially open and open conformations, CSPs on the bottom of Rad50 and on Mre11 (Figs. 1 and 2A) would be expected. Like the side-chain methyl group resonances of Mre11, when hairpin DNA was added to Rad50-labeled MR^{NBD} complex, the peaks in the $Rad50^{NBD}$ spectra were also in fast

exchange (Fig. 2A). However, individual fits of these data to a simple two-state binding model resulted in three distributions of apparent K_Ds (Fig. 2B; Supplementary Data 2). The first apparent K_D had a median of ~3.2 μM (e.g., I25 and I839 in Fig. 2B), similar to the results for Mre11, and was only observed for methyl groups on the 'bottom' of Rad50^{NBD} (Fig. 2B). The second apparent K_D had a median of 27 μM (e.g., I816 and I837) and was obtained for side chain methyl groups within the hydrophobic core (Fig. 2B). The third apparent K_D had a median of 104 μM (e.g., V45 and L89) and was observed from residues on 'top' of Rad50^{NBD} (Fig. 2B). The higher affinity K_D calculated from the methyl groups on 'top' of Mre11 and the 'bottom' of Rad50^{NBD} are consistent with DNA binding to an open conformation of the complex. On the other hand, the lower affinity K_D for the residues on 'top' of Rad50^{NBD} would be consistent with DNA binding to closed MR^{NBD}. This significantly higher K_D than what has previously been reported for closed MR binding to DNA[33,34] could be the result of having to first shift this ATP-free population from an open/partially open conformation to the closed conformation prior to DNA binding.

To determine if the symmetrical chemical shifts observed here are only the result of the small 15 base-pair hairpin DNA being employed, a 50 base-pair DNA duplex, similar in length to the substrates used in the recent cryo-

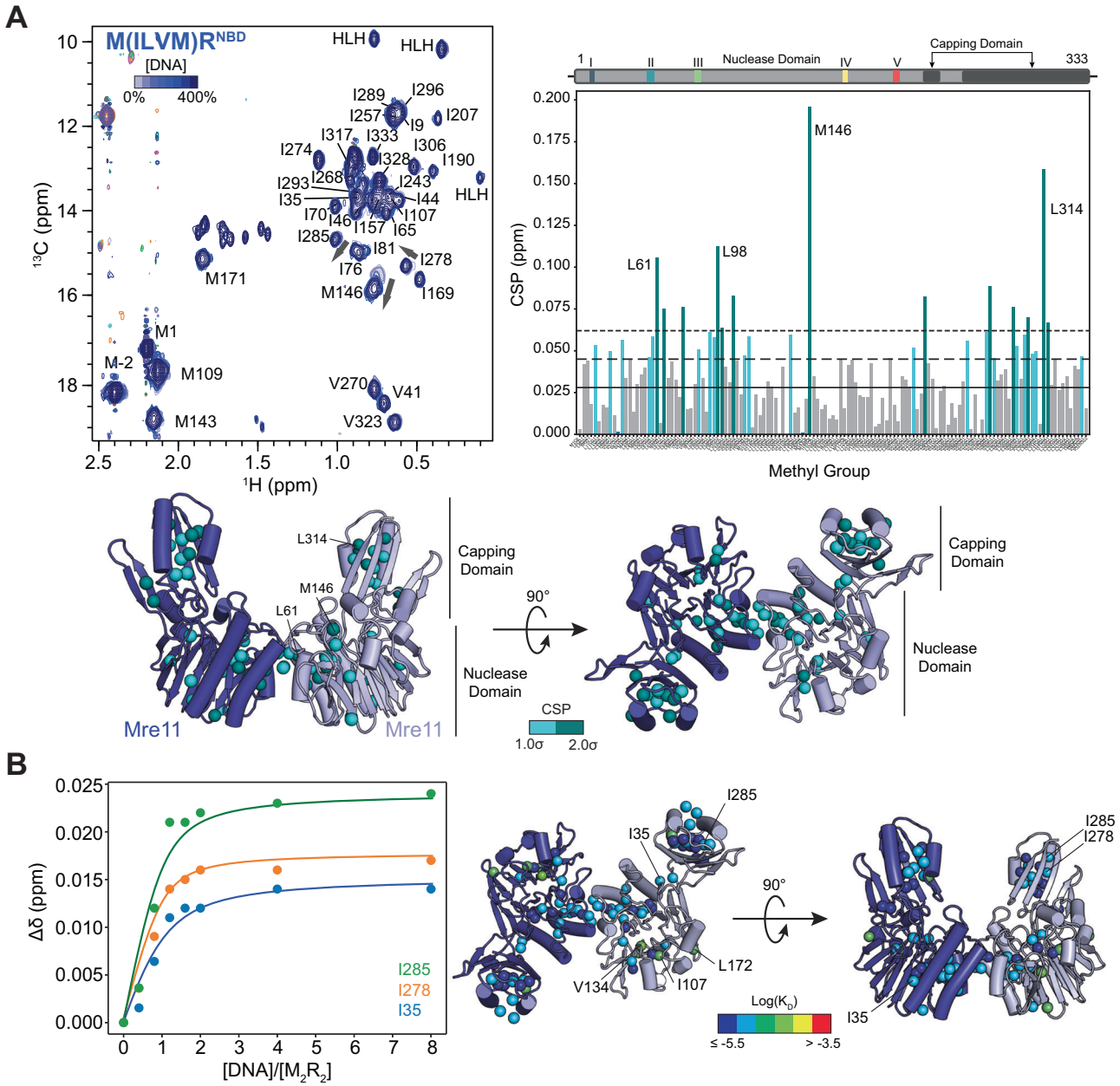

Fig. 1 | dsDNA binds to a single surface on *Pf* Mre11. A Left, overlay of a region from the 2D ^{13}C,^{1}H HMQC spectra of ILVM-labeled Mre11 in complex with Rad50^{NBD} in the presence of increasing hairpin DNA concentration. Blue color gradient indicates the amount of added DNA. Gray arrows highlight several peaks undergoing fast exchange upon the addition of hairpin DNA. Right, bar chart of the CSPs upon DNA binding for each assigned Mre11 methyl group, with horizontal lines indicating the trimmed mean (solid; 0.028 ppm), +1.0 (long dashed; 0.045 ppm), and +2.0 (short dashed; 0.062 ppm) standard deviations, respectively. Below, side-chain methyl groups with dsDNA-dependent Mre11 CSPs between 1.0 and 2.0 standard deviations greater than the trimmed mean CSP are plotted as colored spheres onto the crystal structure of the Mre11ND dimer (PDB ID: 3DSC)[29]. **B** Left, plot of the chemical shift difference for Mre11 side-chain methyl group resonances versus the ratio of the concentrations of DNA to M(ILVM)R^{NBD} complex. Solid lines represent the fit to the data. Right, side-chain methyl groups of Mre11ND (PDB ID: 3DSC)[29] with CSPs above the trimmed mean perturbation plotted as spheres and colored based on the $\log_{10}(K_D)$, where the K_D has units of M. The blue-green-red gradient indicates methyl groups with higher-to-lower affinity for DNA.

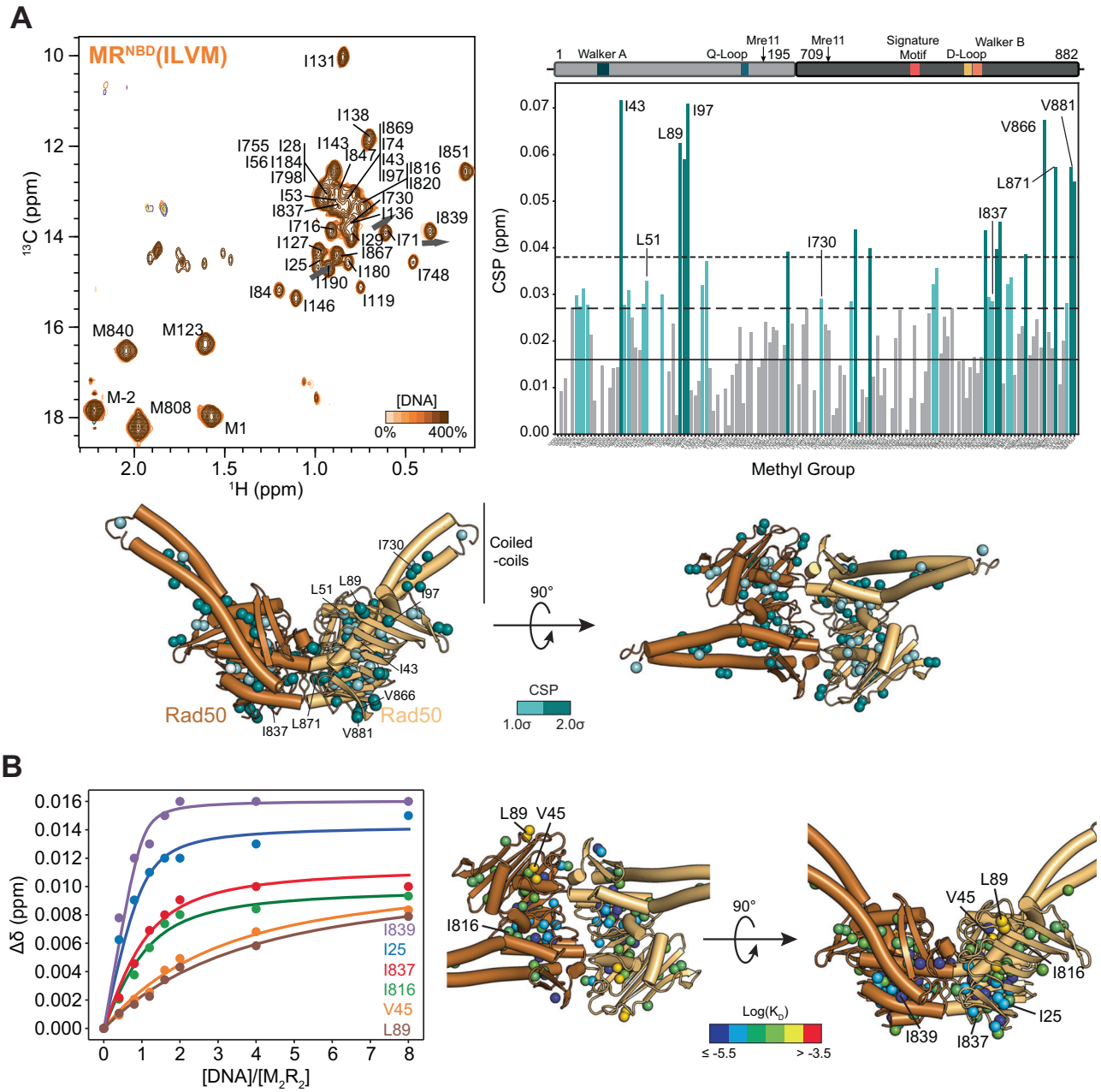

Fig. 2 | dsDNA binds to two surfaces on *Pf* Rad50. A Left, overlay of a region from the 2D ^{13}C,^{1}H HMQC spectra of Mre11 in complex with ILVM-labeled Rad50^{NBD} in the presence of increasing hairpin DNA concentration. Orange color gradient indicates the amount of added DNA. Gray arrows highlight several peaks undergoing fast exchange upon the addition of hairpin DNA. Right, bar chart of the CSPs upon DNA binding for each assigned Rad50 methyl group, with horizontal lines indicating the trimmed mean (solid; 0.016 ppm), +1.0 (long dashed; 0.027 ppm), and +2.0 (short dashed; 0.038 ppm) standard deviations, respectively. Below, side-chain methyl groups with dsDNA-dependent Rad50 CSPs between 1.0 and 2.0 standard deviations greater than the mean CSP are plotted as colored spheres onto the crystal structure of the Rad50^{NBD} (PDB ID: 3KQU)[32] dimer. **B** Left, plot of the chemical shift difference for side-chain methyl group resonances versus the ratio of the concentrations of DNA to MR^{NBD}(ILVM) complex. Solid lines represent the fit to the data. Right, side-chain methyl groups of Rad50 (PDB ID: 3KQU)[32] with CSPs above the trimmed mean perturbation plotted as spheres and colored based on the $\log_{10}(K_D)$, where the K_D originally has units of M. The blue-green-red gradient indicates methyl groups with higher-to-lower affinity for DNA.

EM model determination[38,39], was instead added to Mre11-labeled MR^{NBD} complex (Supplementary Fig. S2). Many residues have weaker intensity in this spectrum as compared to the 15 base-pair spectra suggestive of multiple MR complexes binding to this longer DNA and the entire complex tumbling more slowly in solution. Nevertheless, these data show a single set of peaks and the same CSPs as observed for the hairpin DNA, indicating that *Pf* MR^{NBD} also interacts symmetrically with longer DNAs.

To identify more precisely where the DNA is binding to the MR^{NBD} complex, we next measured PREs between the DNA and complex. The PRE arises from dipolar interactions between a nucleus of interest and the unpaired electron of a paramagnetic center and results in a distance-dependent ($1/r^6$) increase in relaxation rates and line broadening and a decrease in intensities for peaks closer to the label[50,51]. To derive distance restraints between the MR^{NBD} complex and specific nucleotides in the DNA hairpin via the PRE, a paramagnetic spin label was incorporated at various positions (one at a time) in a phosphorothioate-modified hairpin DNA[52]. For example, the phosphorothioate for the '24S' spin label was incorporated at the

twenty-fourth nucleotide from the 5'-end of the DNA (Fig. 3A). PRE line broadening effects were observed in both Mre11-labeled and Rad50^{NBD}-labeled MR^{NBD} complexes upon binding to the spin-labeled DNAs (Fig. 3B, C; Supplementary Fig. S3; Supplementary Fig. S4). Like the CSP data (Figs. 1 and 2), the PRE data also suggest that *Pf* MR^{NBD} binds dsDNA in at least two conformations in solution. For example, when the nitroxide spin label is placed at the second nucleotide from the 5'-end (2S), Mre11 residues I81, M109, L124, M146, and I207 near the nuclease active site are broadened in the Mre11-labeled MR^{NBD} complex (Fig. 3B, Supplementary Fig. S3). And, when that same spin-labeled DNA is added to Rad50^{NBD}-labeled MR^{NBD} complex, residues I180, I716, L719, and L729 in the Rad50 coiled-coil domain near the Mre11 helix-loop-helix (HLH) interaction site are broadened (Fig. 3C; Supplementary Fig. S4). These two regions are ~60-80 Å apart in structures of MR and are therefore incompatible with hairpin DNA(s) binding to a single conformation of the MR^{NBD} complex. Together, the CSP and PRE data are most consistent with dsDNA binding to multiple conformations of MR^{NBD} in solution, which are in equilibrium between various DNA-free and DNA-bound conformations.

The ensemble of MR^{NBD}-dsDNA complexes

Using the CSP and PRE data described above, the High-Ambiguity Driven DOCKing (HADDOCK) v2.4 web server[53–56] was used to construct structural models of the *Pf* MR^{NBD} complex bound to dsDNA[53]. Each HADDOCK calculation was set up to dock a Mre11$_2$-Rad50$^{NBD}{}_2$ complex (the closed, partially open, or open MR^{NBD} structures from our previous LRET studies or an apo [i.e., nucleotide-free] 'closed' MR^{NBD}) with two DNAs. The DNA-bound MR complex was modeled symmetrically bound to two DNAs for several reasons. First, the one set of CSPs can most easily be explained by a DNA binding to a binding site on each Mre11/Rad50 protomer, although our data does not explicitly exclude additional asymmetric binding modes also in fast exchange. Second, several previously reported X-ray crystal structures have two DNAs bound to the Mre11 dimer or a single longer DNA (approximated by two of the DNAs utilized here) binding to either the Mre11 dimer or Rad50 dimer[29,30,33]. Lastly, it was convenient to model symmetrically bound DNA in HADDOCK as it simplified the inputs. Solvent-exposed methyl residues with CSPs greater than 1x the standard deviation above the trimmed mean (Supplementary Fig. S5) and PREs were included as ambiguous and unambiguous distance restraints, respectively (see Supplementary Information for details and rationale).

The lowest energy HADDOCK models for the closed conformations of MR^{NBD} complexes bound to two DNAs (PDB-IHM: 9A9N; Figs. 4A, B and 5A; Supplementary Fig. S6A, B) are very similar to existing crystal structures of closed MR^{NBD}/MR and Rad50^{NBD} dimers, where a single DNA lies across the top of the Rad50 dimer (Supplementary Figs. S1, S7)[33,35,38,39]. In our models, the two hairpin DNAs meet either end-to-end (reduced $\chi^2 = 2.68$; Fig. 4A) or loop-to-loop (reduced $\chi^2 = 2.81$; Supplementary Fig. S6A) in the center of the Rad50 dimer, mimicking one longer DNA, similar to a previously described model based on the X-ray crystal structure and DNA binding data for *C. thermophilum* (*Ct*) Rad50^{NBD} (ref. 35). An apo (nucleotide-free) 'closed' MR^{NBD} DNA-bound model was required to satisfy the Rad50 PREs observed to residues in the coiled-coil region (PDB-IHM: 9A9Q; reduced $\chi^2 = 1.95$; Fig. 4B; Supplementary Data 3). This structure brings the two Rad50 coiled-coils into proximity, mimicking other "rod" shaped structures that have been reported[38,40]. A single DNA was also docked to closed MR^{NBD} using only the solvent-accessible CSP residues on the 'top' of Rad50 (Supplementary Fig. S6B). These four HADDOCK-calculated closed structures overlaid well with each other and with all the other closed MR^{NBD}-DNA structures reported in the literature (Supplementary Fig. S7). Note, the singly bound DNA could appear symmetrical if each Rad50 protomer makes the same sequence-independent contacts with the DNA.

The lowest energy HADDOCK structure for the open conformation of MR^{NBD} bound to two dsDNA (PDB-IHM: 9A9P; reduced $\chi^2 = 1.15$) has the 3'-ends of the DNAs interacting with the active site residues of Mre11 (H52/H85) and positioned next to Mre11 Y187 (Figs. 4C and 5C). A product mimic, AMP, was stacked against this conserved aromatic residue in a crystal structure of *Pf* Mre11ND and mutating this residue severely impairs exonuclease activity[28,49]. The trajectory of the DNA out of the active site leads the minor groove to interact with R90 of the Mre11 nuclease domain of the opposite protomer and continues up to the 'bottom' of the Rad50 NBD where it interacts with CSP residue L871 (Figs. 4C and 5C). This structure builds on a previously determined crystal structure of a DNA-bound *Pf* Mre11ND (Supplementary Fig. S8)[29], where the shorter hairpin DNA (7 bp stem vs 15 bp stem used here) did not access the active site, and with no Rad50 in the complex, the DNA could not be stabilized in the same orientation. Like this previous structure, our open MR^{NBD}-dsDNA structure has Mre11 H17 protruding into the minor groove, consistent with the hypothesis that this 'wedge' residue is poised to participate in DNA unwinding[29]. The 'loops in' open MR^{NBD}-DNA structure (reduced $\chi^2 = 1.11$; Supplementary Fig. S6C) very closely resembles the 'ends in' structure, except the DNA is rotated 180° so the loops of the DNAs are interacting with the Mre11 active site residues, consistent with the recently determined cryo-EM models of *E. coli* (*Ec*) MR bound to blunt and hairpin DNAs[39].

Finally, in our DNA-bound partially open MR^{NBD} model (PDB-IHM: 9A9O; reduced $\chi^2 = 1.19$; Fig. 4D), the 3'-end has exited the active site and is positioned halfway between the Mre11 H17 wedge residue and R833 of the Rad50 dimer interface. Because of the relative conformation of Rad50, the hairpin DNA can no longer fit into the Mre11 active site. The 5'-end of the DNA has moved out of the complex to interact with Q20 of the same Mre11 protomer. The remainder of the DNA lies along the opposite Mre11 nuclease domain, where it contacts several positively charged residues, as well as R868 and the CSP residue V881 on the bottom of the Rad50 NBD. Thus, a different set of Mre11 and Rad50 residues interact with hairpin DNA in the partially open state compared to the DNA-bound open state. In total, seven different structures of hairpin DNA-bound MR^{NBD} are needed to completely satisfy the NMR data (Supplementary Information and Supplementary Data 3).

MR-DNA models reveal interdependence of Mre11 and Rad50 activities

To test whether the proposed MR-dsDNA interactions are important for the function of the MR complex, we generated charge reversal mutants of several positively charged residues close to the DNA in our models and tested their activities in vitro. To probe the DNA-bound closed conformation, a S115E/S116E double mutation on the 'top' of Rad50 was made as well as Rad50 K172E and Mre11 K365E mutations to the coiled-coil and HLH, respectively (Fig. 5A, B). Note, the double serine mutant is analogous to previously described Rad50 mutants that disrupt DNA binding[33,35,38]. To probe the DNA-bound partially open/open conformations, R833E/R834E and R868E mutations on the 'bottom' of Rad50 and Mre11 R87E, R90E, K111E, K144E, and R160E mutations (Fig. 5C, D) were made. LRET experiments established that these mutants could all form MR complex and that all of the complexes closed upon ATP-binding (Supplementary Fig. S9)[43].

In contrast to the NMR studies, we used full-length Rad50, which contains the coiled-coils and Zn hook motifs, in complex with Mre11 for the activity assays. All the mutants based on the partially open and open MR^{NBD}-dsDNA models altered MR binding to a 40 base-pair blunt-ended dsDNA in the absence of ATP (Table 1; Supplementary Fig. S10A), although the majority were within two-fold of the wild type K_D. This result is not surprising given that the Mre11 binding surface is large and mutating a single residue may not have a large effect on DNA binding. The Rad50 double mutant R833E/R834E, which participates in the Rad50 dimer interface with the conserved D829 in the partially open complex, and Rad50 R868E mutant, which interacts with the DNA in partially open complex (Fig. 5D), only slightly increased the K_D of MR for dsDNA in the absence of ATP. This effect was mirrored by the other open/partially open mutants Mre11 K111E,

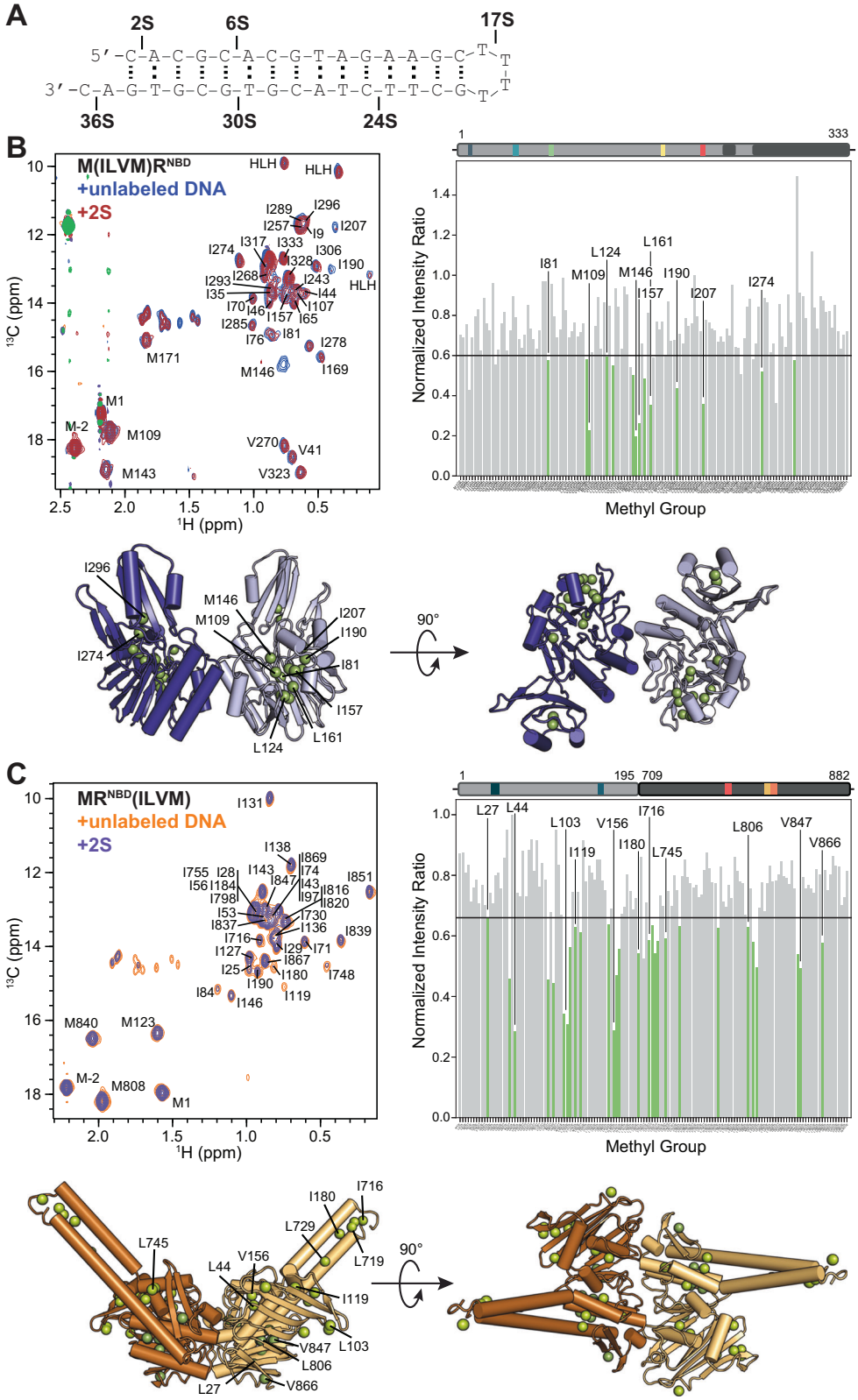

Fig. 3 | PREs from spin-labeled DNA. A Schematic of the hairpin DNA used in the NMR studies with the position of each paramagnetic spin label indicated. **B** and **C** Left, overlay of a region from the 2D ^{13}C,^{1}H HMQC spectra for M(ILVM)R^{NBD} (**B**) and MR^{NBD}(ILVM) (**C**). Data collected with unlabeled or 2S PROXYL-labeled DNA are represented by blue and red (**B**) and orange and blue (**C**) contours, respectively. **B** and **C** Right, bar chart of the normalized intensity ratio (spin-label/no label) for Mre11 (**B**) and Rad50^{NBD} (**C**) methyl group resonances for the 2S PROXYL-labeled DNA. The green shaded bars for methyl groups below the horizontal line were used for HADDOCK inputs. **B** and **C** Below, methyl groups below the horizontal lines in the bar charts are shown as green spheres on the crystal structure of Mre11ND dimer (PDB ID: 3DSC)[29] (**B**) and Rad50^{NBD} (PDB ID: 3KQU)[32] dimer (**C**).

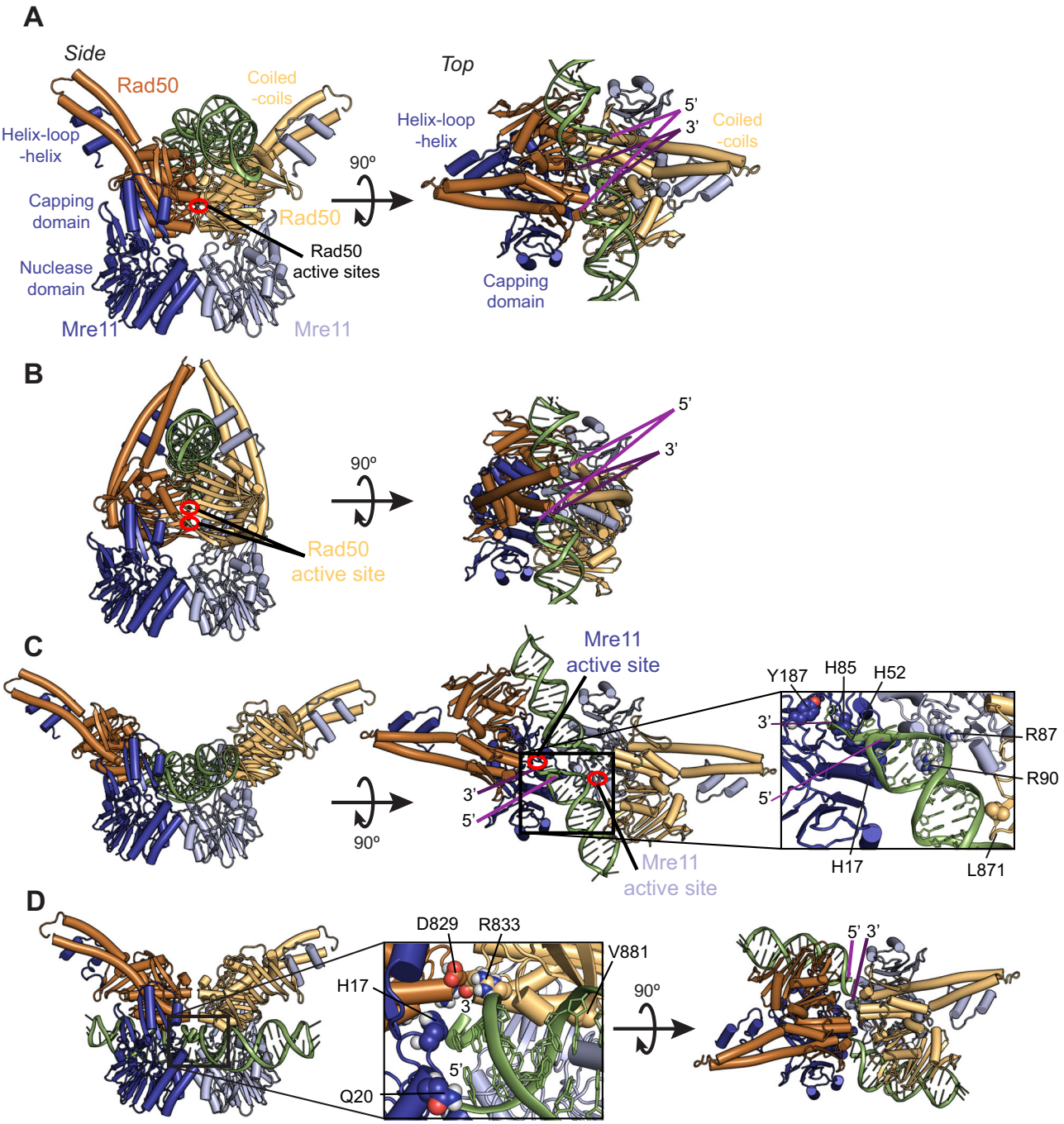

Fig. 4 | dsDNA-bound MR^{NBD} adopts an ensemble of heterogeneous conformations in solution. A The closed MR^{NBD}-dsDNA structure where the 5'- and 3'-ends of two hairpin DNAs meet in the middle of the Rad50 dimer. **B** The closed apo (no ATP) MR^{NBD}-dsDNA structure where the Rad50 coiled-coils and Mre11 helix-loop-helix (HLH) motif are close to the DNA. **C** The open MR^{NBD}-dsDNA structure with the 3'-end of the DNAs at the Mre11 active sites. **D** The partially open MR^{NBD}-dsDNA structure where the helix of the hairpin is interacting with the Mre11 nuclease domain and the bottom of Rad50. A side view and a top view are presented for each structure and a number of contacts between DNA and Mre11 or Rad50 are highlighted in the insets of **C** and **D**.

K144E, and R160E mutants, with K144E having the greatest increase in K_D at ~3.6-fold. Conversely, the Mre11 mutants R87E and R90E both nearly abolished dsDNA binding to MR. Based on our structural models, these two arginine residues are on either side of a DNA strand in the partially open MR^{NBD}-dsDNA complex (Fig. 5D). Additionally, R90 contacts the DNA in the open complex (Fig. 5C). In fact, of the residues mutated, R90 is the only one to contact the DNA in both partially open and open conformations, perhaps explaining the deleterious effect of reversing its charge. In the closed conformation of the MR^{NBD}-dsDNA complex, Rad50 residues S115 and S116 on a strand-loop-helix motif interact with the dsDNA (Fig. 5A, B). Equivalent residues were previously shown to affect dsDNA binding in *M. jannaschii* (*Mj*), *T. maritima* (*Tm*), *Ec*, and *Ct* Rad50^{NBD} dimer or MR complexes[33,35,38]. Here, the S115E/S116E Rad50 double mutant showed wild-type binding to dsDNA in the absence of ATP (Table 1; Supplementary Fig. S10A). This contrasts with the equivalent mutant in full-length *Tm* MR (R94E/K95E) which binds dsDNA less efficiently than wild type in both the presence and absence of ATP[33]. In the Pf MR^{NBD} complex, the S115E/S116E mutant binds to dsDNA with the same affinity as wild type in the absence of ATP but binds less efficiently in the presence of ATP (Supplementary Fig. S10B), as was observed for the *Mj* MR^{NBD} and *Ct* Rad50^{NBD} mutants[33,35].

Table 1 | . Activity assay data for wild type and mutant MR complexes

	dsDNA binding, No ATP[b]		Nuclease	ATP hydrolysis			ATP hydrolysis with plasmid DNA			
MR mutant[a]	K_D (μM)	Hill	pmol /min	Vmax[c]	Hill	K_M (μM)	Vmax[c]	Hill	K_M (μM)	Fold stim[d]
Wild type	0.59 ± 0.05	1.5 ± 0.2	0.137 ± 0.009	5.0 ± 0.1	1.5 ± 0.1	20.4 ± 1.0	64.0 ± 1.8	1.7 ± 0.1	36.7 ± 1.9	12.8
S115E/S116E (R)	0.58 ± 0.06	1.3 ± 0.2	0.026 ± 0.001	4.9 ± 0.2	1.7 ± 0.2	22.7 ± 1.7	7.2	1.4	27.9	1.5
K172E (R)	0.58 ± 0.03	1.8 ± 0.2	0.116 ± 0.001	3.8 ± 0.2	1.2 ± 0.1	19.1 ± 1.9	45.1	1.6	32.8	11.9
K365E (M)	0.71 ± 0.05	1.4 ± 0.1	0.098 ± 0.002	4.2 ± 0.3	1.3 ± 0.2	21.1 ± 2.6	44.9 ± 3.4	1.2 ± 0.2	36.6 ± 6.4	10.7
R833E/R834E (R)	1.08 ± 0.13	1.3 ± 0.2	0.069 ± 0.004	10.5 ± 0.3	1.7 ± 0.1	29.5 ± 1.7	17.3 ± 1.0	1.2 ± 0.1	43.9 ± 5.9	1.6
R868E (R)	0.75 ± 0.07	1.4 ± 0.2	0.068 ± 0.003	5.8 ± 0.1	1.9 ± 0.1	23.6 ± 1.0	60.1 ± 2.0	1.6 ± 0.1	31.9 ± 2.0	10.4
R87E (M)	N/D	N/D	0.223 ± 0.007	3.2 ± 0.1	1.0 ± 0.1	18.9 ± 2.1	7.6	1.3	3.8	2.4
R90E (M)	N/D	N/D	0.234 ± 0.004	2.6 ± 0.1	1.9 ± 0.3	10.9 ± 0.8	82.4	1.3	54.0	31.7
K111E (M)	1.07 ± 0.11	1.4 ± 0.2	0.288 ± 0.007	2.5 ± 0.1	1.8 ± 0.2	14.5 ± 1.1	71.2	1.6	37.0	28.5
K144E (M)	2.12 ± 0.42	1.3 ± 0.2	0.215 ± 0.002	1.8 ± 0.1	1.5 ± 0.2	10.9 ± 1.2	47.7	1.3	46.1	26.5
R160E (M)	0.96 ± 0.06	1.5 ± 0.1	0.273 ± 0.015	3.4 ± 0.1	1.8 ± 0.2	11.6 ± 0.9	70.5	1.3	42.8	20.7

[a]Mre11 and Rad50 mutants in the MR complex are designated by (M) and (R), respectively. Mutants designed to disrupt 'closed' MR-DNA interactions are bolded: S115E/S116E (R), K172E (R), and K365E (M). Mutants designed to disrupt 'partially open' and 'open' MR-DNA interactions are: R833E/R834E (R), R868E (R), R87E (M), R90E (M), K111E (M), K144E (M), and R160E (M).

[b]dsDNA binding affinity to full-length MR in the absence of ATP. Errors are SEM of $n = 3$ independent experiments.

[c]pmol PO_4/min. Values without error bars are the average of $n = 2$ independent experiments, while values reporting a SEM are the result of $n = 3$ independent experiments.

[d]Fold stimulation of ATP hydrolysis activity as a result of linearized plasmid DNA in the reaction. Calculated using the Vmax from each condition.

Two positively charged residues in the Rad50 coiled-coil:Mre11 HLH interface that are close to the DNA in our 'rod' shaped closed apo MR^{NBD}-dsDNA model were also mutated: Rad50 K172 and Mre11 K365 (Fig. 5B, bottom). Mutating either of these lysine residues to glutamic acid (i.e., K172E and K365E) in full-length MR did not affect dsDNA binding in the absence of ATP as compared to wild type (Table 1; Supplementary Fig. S10A), but these mutants in MR^{NBD} both showed a decrease in binding with respect to wild type when ATP was present (Supplementary Fig. S10B). These ATP-dependent DNA binding data are consistent with our proposed structures and model of conformational exchange. In the absence of ATP, we hypothesize that the open/partially open states are more highly populated. Since the open/partially open DNA binding sites (i.e., the Mre11 binding site) are intact for the Rad50 S115E/S116E, Rad50 K172E, and Mre11 K365E mutant complexes, the DNA can bind to Mre11 and binding is similar to wildtype. On the other hand, in the presence of ATP, the closed state is now more populated, which occludes the open/partially open Mre11 DNA binding site, and since the closed binding sites on Rad50 are mutated, DNA binds with less affinity for these Rad50 mutant complexes in the presence of ATP.

Next, MR nuclease activity was assayed in a fluorescence-based assay with a blunt-ended 29 base-pair dsDNA. For the partially open/open charge reversal mutants, two different effects were observed: Rad50 mutants R833E/R834E and R868E decreased nuclease activity of MR by 50%, whereas Mre11 mutants R87E, R90E, K111E, K144E, and R160E all increased nuclease activity to ~150-200% of wild type (Fig. 5E; Table 1). For the closed mutants, Rad50 K172E and Mre11 K365E near the coiled-coil:HLH interface decreased nuclease activity by ~15% and ~30%, respectively. And, as previously reported, the Rad50 S115E/S116E mutant abolished 80% of MR nuclease activity[33,38]. These nuclease results were confirmed in a polyacrylamide gel-based assay (Supplementary Fig. S11), where the overall cleavage of the dsDNA substrate by the mutant MR complexes mirrors what was observed in the fluorescence-based nuclease assay. Interestingly, a near total loss of endonuclease activity was observed in the Rad50 S115E/S116E mutant; however, this mutant was still capable of some exonuclease activity (Supplementary Fig. S11). On the other hand, all the partially open/open Mre11 mutants displayed increased nuclease activity, particularly against the exonuclease substrate. The increased activity was exemplified by a Mre11 R87E/R90E double mutant, which completely degraded the substrate. Differences in the cleavage pattern of the exonuclease substrate strand (i.e., more shorter products) suggest that the Mre11 partially open/open mutants can perform extra processive exonuclease activity (Supplementary Fig. S11).

Finally, the hydrolysis of ATP by Rad50 was assessed in each of the mutant MR complexes (Fig. 5F; Table 1). Opposite of the nuclease results, Rad50 R833E/R834E and R868E both increased the V_{max} of hydrolysis, whereas the Mre11 mutants all decreased V_{max}. Like the DNA binding results, many of these changes were within two-fold of wild type. The MR complex displays V-type allostery, with the rate of ATP hydrolysis increasing by about 10-fold in the presence of a long, linearized dsDNA[21,38,40,42,46,57]. The major effect of the mutations on ATP hydrolysis was observed in this context. For the partially open/open Mre11 mutants, apart from R87E, the lower-than-wild type ATP hydrolysis activity was greatly stimulated by linearized plasmid DNA, with V_{max} increasing 20- to 30-fold over that in the absence of DNA (Fig. 5F; Table 1). Conversely, the Mre11 mutant R87E showed only two-fold stimulation of ATP hydrolysis upon the addition of linearized plasmid. Rad50 R868E showed significant stimulation of activity in the presence of linear DNA, though not quite to the level of wild type (10.4-fold vs 12.8-fold), whereas the R833E/R834E MR hydrolysis activity was not stimulated at all. In the closed mutant MRs, hydrolysis by the Rad50 S115E/S116E mutant MR was also not stimulated by DNA, as expected based on previously published results for *Ec* MR[38]. And, although Rad50 K172E and Mre11 K365E MRs showed a slight decrease in ATP hydrolysis activity without DNA as compared to wild type, they approached wild-type-like stimulation when linearized plasmid was added to the reactions (12- and 10-fold, respectively). In total, the nuclease and ATP hydrolysis activity assay results validate the various DNA-bound MR^{NBD} structures detected in solution and demonstrate that the protein-nucleic acid interactions observed in the ensemble of MR^{NBD}-dsDNA structures are important for MR function.

Discussion

The Mre11-Rad50 complex is a universally conserved and essential DNA end sensing and processing machine that helps to prime the ends of DNA DSBs for subsequent repair by NHEJ and HR[6,7]. Even with the multitude of structures available (Supplementary Fig. S1), a coherent description for the structure-function relationship and the interplay of enzymatic activities of the MR complex is lacking. Here, we utilized sensitive side-chain methyl

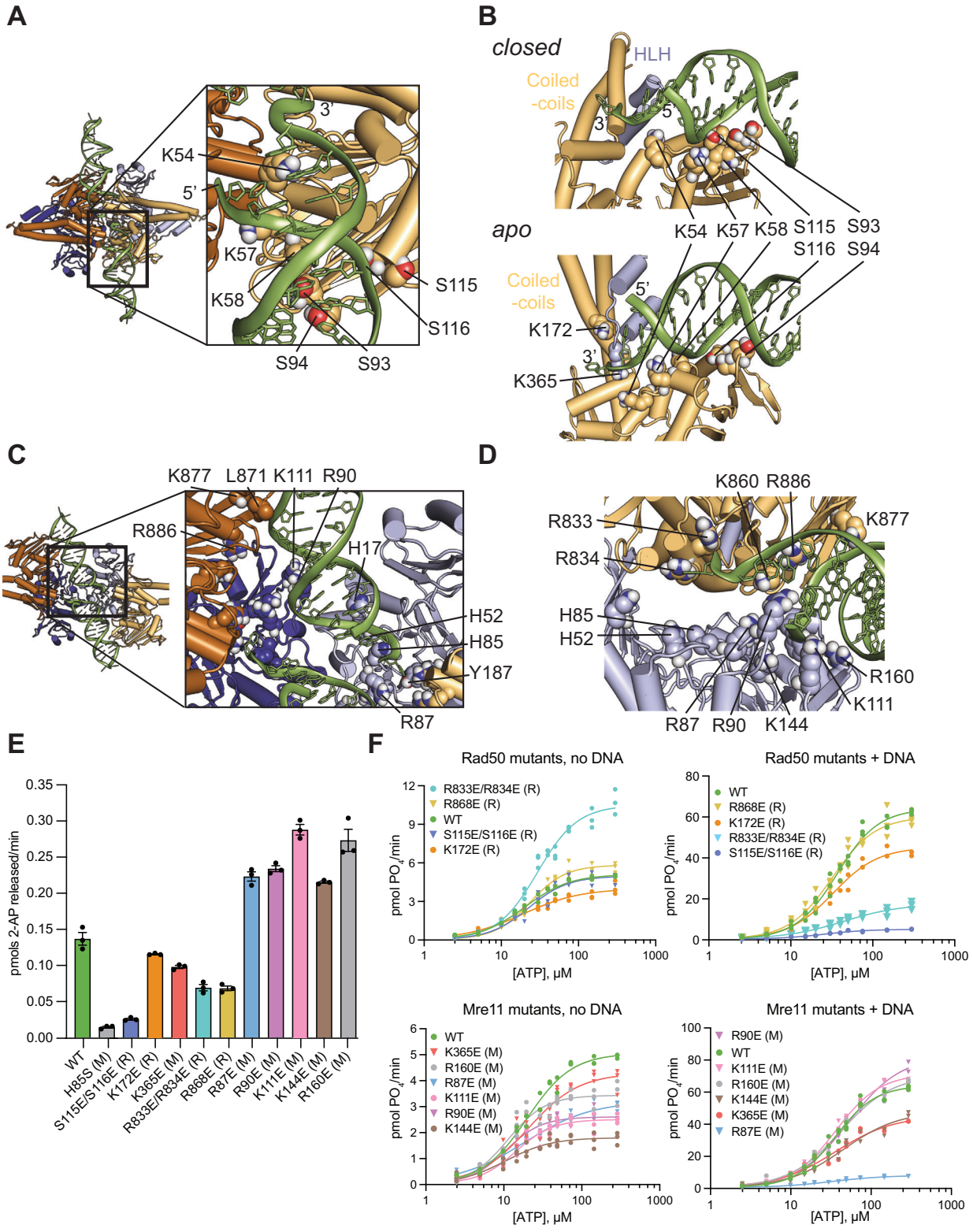

Fig. 5 | Disrupting MR^{NBD}-dsDNA interactions affects MR functions. A Top view of the closed MR^{NBD}-dsDNA structure with an expanded view of the polar contacts between Rad50 and the hairpin DNA. **B** Side view of the closed (top) and apo closed (bottom) MR^{NBD}-dsDNA structures highlighting polar contacts. **C** Top view of open MR^{NBD}-dsDNA structure with an expanded view of the polar contacts between MR and the DNA and Mre11 active site residues H52 and H85. **D** Side view of partially open MR^{NBD}-dsDNA structure showing polar contacts. **E** Results of the fluorescence assay for the nuclease activity of mutant MR complexes plotted as a pmols 2-AP released per min. Mre11 and Rad50 mutants are designated by (M) and (R), respectively. Mre11 H85S is a nuclease-deficient mutant. Error bars indicate the SEM of $n = 3$ independent experiments. **F** ATP hydrolysis activity of mutant MR complexes plotted as a function of ATP concentration in the absence (left) and presence (right) of linearized plasmid dsDNA. Data from $n = 3$ (without DNA) or $n = 2$ (with DNA) independent experiments were fitted by Prism to the Michaelis-Menten equation, including a Hill coefficient. The solid line represents the fit, and the fitted V_{max}, Hill coefficient, and K_m values are reported in Table 1.

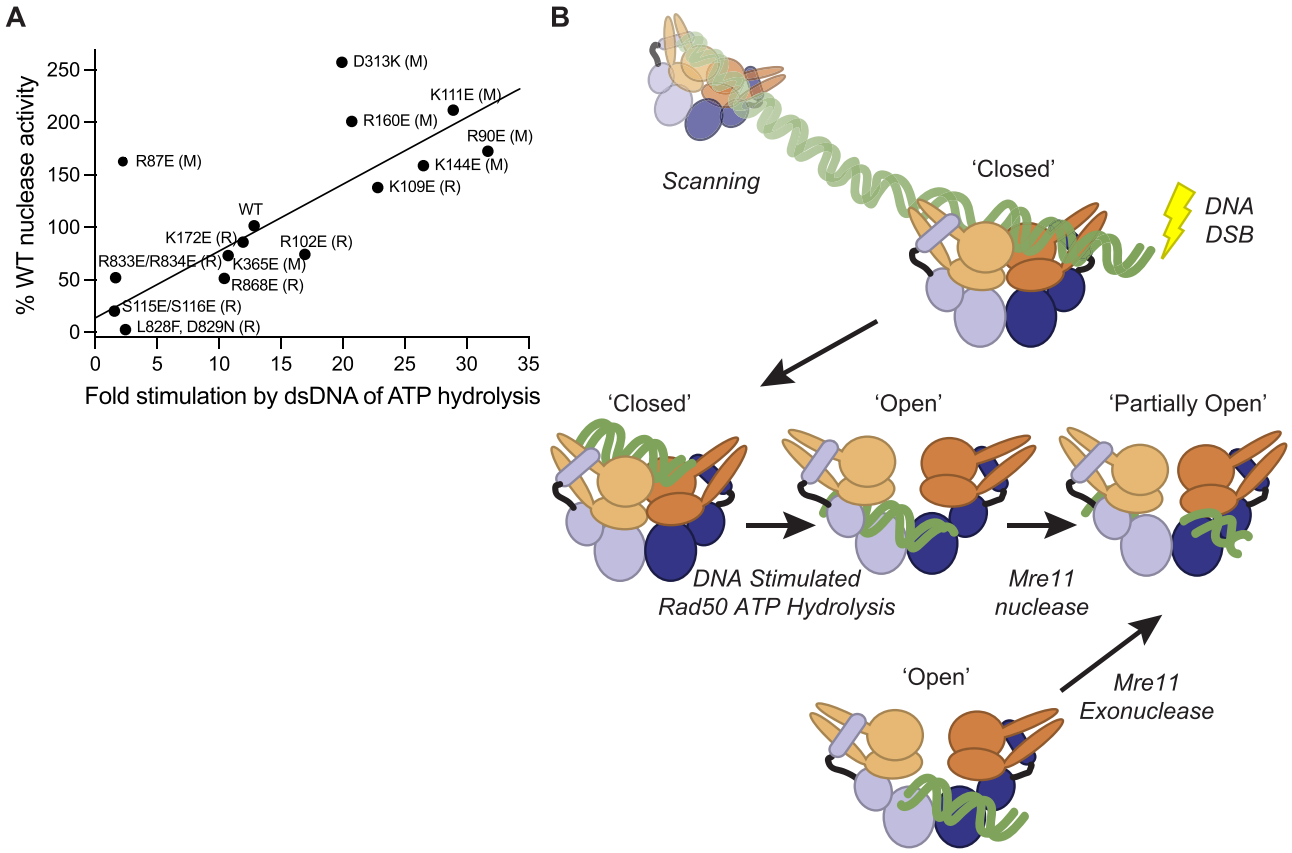

Fig. 6 | Correlation of MR activities suggests a model for MR function. **A** Correlation between Mre11 exonuclease activity, expressed as a percentage of wild type, and fold stimulation of Rad50 ATP hydrolysis activity from the presence of linearized DNA. **B** Model for MR activity where MR scans the DNA for damage which results in stimulation of Rad50 ATP hydrolysis to expose the Mre11 active site for nuclease activity. Additional exonuclease activity can occur directly from the open conformation. Product dsDNA is excluded from the Mre11 active site as the complex forms the partially open state.

group NMR experiments to characterize MR^{NBD} conformational exchange and determine models of a dynamic ensemble of dsDNA-bound *Pf* MR^{NBD} complexes in the absence of ATP. Based on these models, charge reversal mutants were used to validate the ensemble. Even though ATP was omitted in our structural analysis, the mutants derived from these structures produced dramatic effects on ATP-dependent Mre11 nuclease and Rad50 ATP hydrolysis activities. Surprisingly, analysis of the activity assay data uncovered a strong correlation between the dsDNA-stimulated Rad50 ATP hydrolysis activity and Mre11 nuclease activity (Fig. 6A) demonstrating the importance of this ensemble on MR function.

Together, our ensemble of solution-state structural models and activity assay data support a model for MR activity that was previously proposed by Cho and co-workers (Fig. 6B)[33], with our structural models of partially open and open MR^{NBD} bound to DNA providing missing structures within the proposed functional model. In this functional model, dsDNA binds to the closed conformation of MR either in the presence or absence of ATP. Closed MR scans the DNA looking for a DNA DSB, as demonstrated by single-molecule fluorescence measurements that showed efficient scanning in a nucleotide-independent manner[44]. When MR encounters a break, Rad50 ATP binding (if necessary) and hydrolysis activity is allosterically stimulated, which shifts the population from the closed to open conformation, where Mre11 can now perform endonuclease activity. As part of this transition, the dsDNA is engaged by Mre11 H17 and R90, which along with previously characterized motions of the Mre11 capping domain[29,43], may partially unwind the dsDNA. After nuclease activity, cleaved product is excluded from the Mre11 active site as the global conformation of the MR complex equilibrates to the partially open state. Biologically, it is logical that a DNA DSB should activate Rad50 ATP hydrolysis activity – in this scenario, the Mre11 active site remains occluded while scanning the DNA and does not become available until a break is encountered and nuclease activity is needed. Thus, allosterically activated ATP hydrolysis unlocks the Rad50 gate to the Mre11 active site. But what is the mechanism that underlies this regulation?

This model suggests that Rad50 somehow senses the end of the dsDNA helix. We have previously used methyl-based NMR data to describe three clusters of residues in *Pf* $Rad50^{NBD}$ that constitute two different allosteric networks within the Rad50 NBD[58]. Methyl NMR data on a series of mutants correlated with Rad50 dimerization, ATP hydrolysis, and Mre11 exonuclease activity for two of these clusters. We hypothesize that the third cluster, which encompasses a hydrophobic cavity that collapses upon ATP binding[16,32], could be responsible for transmitting the allosteric DNA binding to the Rad50 active site. In fact, hairpin DNA-induced CSPs were observed to many of these same solvent-inaccessible methyl groups (Fig. 2A), and these methyl groups largely fit to the intermediate apparent K_D in our DNA titration data (Fig. 2B). This binding constant could be reporting on the shift in equilibrium within the core of Rad50 that is necessary for ATP hydrolysis[16,32,58]. Additionally, as DNA end tethering by MR can occur in the ATP-bound or ATP-free states of MR[16,45], it is unclear which conformation harbors that function. Given that Rad50 mutants incapable of dimerization (*Sc* S1205R and *Pf* L802W) can tether DNA ends[16,45], we propose that end tethering likely results from the partially open or open structures proposed here.

A notable exception to the correlation between Mre11 nuclease activity and Rad50 DNA-stimulated ATP hydrolysis activity is the Mre11 R87E mutant (Table 1; Fig. 6A). Mre11 R87 is near the catalytic H85 and the deviation from the correlated activities observed here is likely the result of the R87E mutant disrupting the local environment of H85. Rad50 R833 and

R834 are on the helix following the conserved ABC ATPase D-loop motif. A previous study of *Pf* MR D-loop mutants L828F and D829N also showed greater background ATP hydrolysis, little DNA-stimulated ATP hydrolysis, and reduced nuclease activity[42] as observed here for R833E/R834E, and the D-loop mutants are also found in the lower left corner of our activity assay correlation (i.e., low exonuclease activity and little stimulation of ATPase activity; Table 1; Fig. 6A). For the D-loop mutants, methyl-based NMR studies attributed the loss in dsDNA-stimulated ATP hydrolysis activity to the disruption of an allosteric network within Rad50 that accelerated ATP hydrolysis, by shifting the equilibrium away from the closed conformation, but decoupled DNA-mediated allosteric activation; we suggest the same may be occurring in the R833E/R834E mutant. Interestingly, the Mre11 D313K mutant, which was originally designed to perturb the closed and partially open states, led to decreased background ATP hydrolysis activity[43]. However, for D313K the opposite effects to the D-loop mutants in the presence of dsDNA (i.e., high exonuclease activity and greater stimulation of ATPase activity; Table 1; upper right of Fig. 6A) were observed. We hypothesize that dsDNA binding to the D313K mutant successfully stabilizes the closed form, and with a functional Rad50 allosteric network, dsDNA-stimulation of ATP hydrolysis activity can occur leading to the observed nuclease activity. Finally, the mutants designed here to disrupt DNA binding to the closed conformation (Rad50 S115E/S116E, Rad50 K172E, and Mre11 K365E) interestingly resulted in less nuclease activity compared to wild type, with the effect being somewhat greater for the endonuclease substrate compared to the exonuclease substrate (Supplementary Fig. S11). This observation suggests that dsDNA binding directly to the population of open MR^{NBD} can result in Mre11 3'-to-5' exonuclease activity.

The models of dsDNA-bound ATP-free MR^{NBD} complex presented herein complement most of the existing structural biology studies on this conserved and essential DNA DSB repair assembly (Supplementary Figs S1, S7, S8). As first reported by Tainer and co-workers in their X-ray crystal structure of $Mre11^{ND}$ bound to DNA DSB mimics[29], our models of the open MR^{NBD} complex are also bound to two DNAs, which lay symmetrically across the Mre11 dimer and engage with the H17 'wedge' residue and capping domain (Fig. 4C; Supplementary Figs. S1, S8). Because our models include $Rad50^{NBD}$, we have identified and confirmed via activity assays using charge reversal mutants that the 'bottom' of Rad50 also plays a role in the stability of this DNA-bound state. Similarly, our model of closed MR^{NBD} shows dsDNA binding across the 'top' of Rad50 in an orientation first observed in the X-ray crystal structures reported by Cho and Hopfner and co-workers (Figs. 4A, B; Supplementary Fig. S7)[33,35]. And the presence of a 'closed' conformation of ATP-free MR was recently reported in the cryo-EM structure of a thermophilic eukaryotic MR complex by Hopfner and co-workers[40]. From these observations, we suggest that all these conformers are present in the solution. On the other hand, the models presented herein contrast with the recent cryo-EM models of ADP-bound *E. coli* MR (i.e., SbcCD) in complex with various nuclease substrates (Supplementary Fig. S1)[38,39]. The most striking difference lies in the asymmetric nature of the cryo-EM models where the Rad50 protomers and the DNA substrate both interact asymmetrically with the Mre11 dimer[38,39]. Although we modeled the DNA-MR interactions symmetrically (largely for ease with HADDOCK), our NMR data, which is in fast exchange on the chemical shift timescale, does not necessarily exclude asymmetric DNA binding. For example, our data would also be consistent with one protomer of MR adopting an open conformation and interacting with the DNA in its mode while the other protomer adopts a partially open conformation and interacts with DNA in that mode at the same time.

Recently, AlphaFold2 was used to model the structure of truncated *S. cerevisiae* (*Sc*) Mre11-Rad50-Sae2 complexes[59]. In vitro and in vivo activity assays of mutants based on these models suggested that *Sc* MR may also adopt an asymmetric 'cutting' state conformer as seen in *Ec*[38]. We therefore wondered what conformation AlphaFold would generate for human (*Hs*) and *Pf* MR complex. Using AlphaFold3 (AF3)[60], we generated models of *Pf*, *Ec*, *Sc*, and *Hs* full-length MR complex in the absence of substrates and in the presence of ATP (the so-called 'resting' state), 40-mer dsDNA (similar to conditions used here), or 40-mer dsDNA and ADP (as observed in the *Ec* 'cutting' state) (Supplementary Fig. S12). In all cases, for apo MR, AF3 predicted a closed conformation, which we observed in previous LRET data for truncated and full-length apo *Pf* MR[43]; for *Ec*, *Pf*, and *Sc* the Rad50 coiled coils were in a rod shaped conformation, whereas the coils were open for *Hs* RAD50 (Supplementary Fig. S12A). In the presence of Mg^{2+}•ATP, AF3 predicted a closed state with open coils for *Pf* and *Hs* or rod coils for *Ec*, whereas the *Sc* MR in the presence of ATP adopted the 'cutting' state, as recently described[59] (Supplementary Fig. 12B). Note, a difference in the Rad50 coiled-coils was also observed in the cryo-EM models of *Ec* and *Ct* MR in the presence of ATPγS[38,40]. When a 40-mer dsDNA was added in the absence of nucleotide, AF3 predicts that the dsDNA will interact on top of closed Rad50 for *Ec*, *Pf*, and *Hs* MR, which is consistent with our CSP (Fig. 2) and PRE data (Fig. 3). On the other hand, AF3 predicted a model for the *Sc* MR-dsDNA complex intermediate to the 'cutting' state (Supplementary Fig. 12C). Finally, when Mg^{2+}•ADP and the 40-mer dsDNA were included in AF3, a closed conformation with the DNA on top of Rad50 with rod coils (*Ec*; in contrast to the cryo-EM model[38]) or open coils (*Hs*), the 'cutting' state (*Sc*), or a novel arrangement with an inverted Rad50 and DNA interacting with the 'top' of closed Rad50 and both Mre11 active sites (*Pf*) is observed. In total, this comparison highlights the potential and pitfalls of modeling large, complicated complexes, supports the possibility that MR may have diverged in the way that it recognizes DNA substrates, and demonstrates the power of solution-state techniques in probing conformational ensembles.

Utilizing one of the strengths of NMR spectroscopy – its sensitivity to sparsely populated states – we characterized an ensemble of conformations present within the ~200 kDa DNA-bound MR^{NBD} complex. Because these various conformations are rapidly exchanging at equilibrium, presumably with their DNA-free forms, their effects are manifested as perturbations in the side-chain methyl group resonance position and marginal loss of intensity due to the PRE. Unfortunately, we cannot obtain the kinetics or thermodynamics of the conformational exchange from our present data; however, it is an avenue that we are currently exploring. Due to the complex nature of the MR complex, we suggest that the structural models reported here provide a framework for the many possible symmetric and asymmetric MR-DNA interactions and add to the myriad of ways that MR can bind to DNA. We were able to use these models to design mutants that disrupt some of the interactions between MR and DNA. These mutants illuminated for the first time a direct coupling between the allosteric activation of Rad50 ATPase activity and Mre11 nuclease function. From these structural models and the associated activity assay data, it is clear is that the MR complex samples a dynamic, heterogeneous ensemble of structures to perform its biological functions that are necessary for DNA DSB repair.

Materials and methods

Protein expression and purification

All point mutations were introduced using a modified QuikChange (Agilent) approach and were verified by Sanger sequencing. Plasmids for *P. furiosus* (*Pf*) Mre11 or *Pf* $Rad50^{NBD}$ (aa 1-195 – GGAGGAGG linker – aa 709-882) expression were transformed into *E. coli* BL21(DE3) C41 cells (Millipore-Sigma) and grown in LB media. Unlabeled protein expression was induced with 1 mM IPTG at 37 °C for 3-4 h. To prepare U- ^{2}H, Ileδ1-[$^{13}CH_3$], Leuδ/Valγ-[$^{13}CH_3/^{12}CD_3$], Metε-[$^{13}CH_3$] (ILVM)-labeled *Pf* Mre11 and *Pf* $Rad50^{NBD}$ protein for NMR spectroscopy, cells were grown in deuterated 2x M9 minimal media[61] with 1 g/L $^{14}NH_4Cl$ and 3 g/L $^{2}H,^{12}C$-glucose as the sole nitrogen and carbon sources, respectively. 100 mg/L of each $^{13}CH_3$-labeled Ile, Leu, Val, and Met metabolic precursor (Cambridge Isotope Laboratories, Inc) were added to the media 45 min prior to induction with 1 mM IPTG[62]. Isotopically labeled proteins were then overexpressed for ~16 h at 37 °C (Mre11) or 25 °C ($Rad50^{NBD}$). Plasmids for full-length *Pf* Rad50 expression were transformed into BL21(DE3)

Rosetta competent cells (Novagen) and grown in LB media. Expression was induced with 0.3 mM IPTG at 18 °C overnight.

Mre11-expressing cells were pelleted and then resuspended in Mre11 lysis buffer (50 mM sodium phosphate, 300 mM NaCl, 25 mM imidazole, pH 8) plus 0.5% (v/v) Tween-20 and 0.5% (v/v) deoxycholate. Cells were disrupted via sonication and then heated at 65 °C for 20 min. The lysate was cleared by centrifugation and the soluble fraction was loaded onto a 5 mL HisTrap HP column (Cytiva). Mre11 was eluted in 50 mM sodium phosphate, 300 mM NaCl, 300 mM imidazole, pH 8. The 6x His-tag was removed with TEV protease, and the protein was dialyzed into 25 mM HEPES, 300 mM NaCl, 25 mM imidazole, pH 7. Cleaved Mre11 was purified as the flow through from the HisTrap column in the dialysis buffer. The sodium chloride concentration was then reduced to 100 mM and the protein sample was further purified on a HiTrap Q HP column (Cytiva) in a linear gradient into 25 mM HEPES, 1 M sodium acetate, 0.1 mM EDTA, pH 7. The sample was concentrated in a 30 kDa MWCO centrifugal concentrator (Sartorius) and loaded onto a HiLoad 16/60 Superdex 200 pg column (Cytiva) equilibrated in 25 mM HEPES, 200 mM sodium acetate, 0.1 mM EDTA, pH 7.

Rad50^{NBD}-expressing cells were pelleted and then resuspended in Rad50^{NBD} lysis buffer (25 mM HEPES, 300 mM NaCl, 25 mM imidazole, pH 7). Cells were disrupted via homogenization (Avestin) and then heated at 65 °C for 20 min. The lysate was cleared by centrifugation and the soluble fraction was loaded onto the HisTrap column. Rad50^{NBD} was eluted in 25 mM HEPES, 300 mM NaCl, 300 mM imidazole, pH 7. The 6x His-tag was removed with TEV protease, and the protein was dialyzed back into Rad50^{NBD} lysis buffer. Cleaved Rad50^{NBD} was purified as the flow through from the HisTrap column in Rad50^{NBD} lysis buffer. The sodium chloride concentration was then reduced to 80 mM and the protein sample was further purified on a HiTrap SP HP column (Cytiva) in a linear gradient into 25 mM HEPES, 1 M sodium acetate, 0.1 mM EDTA, pH 7. The sample was concentrated in a 30 kDa MWCO centrifugal concentrator (Sartorius) and loaded onto a HiLoad 16/60 Superdex 200 pg column (Cytiva) equilibrated in 25 mM HEPES, 200 mM sodium acetate, 0.1 mM EDTA, pH 7.

Full-length Rad50-expressing cells were pelleted and then resuspended in full-length Rad50 lysis buffer (50 mM sodium phosphate, 300 mM KCl, 25 mM imidazole, 10% glycerol, pH 8) plus 0.5% (v/v) Tween-20. Cells were disrupted via sonication and then heated at 65 °C for 20 min. The lysate was cleared by centrifugation and the soluble fraction was loaded onto the HisTrap column. Full-length Rad50 was eluted in 50 mM sodium phosphate, 300 mM KCl, 300 mM imidazole, 10% glycerol, pH 8. The 6x His-tag was removed with TEV protease, and the protein was dialyzed back into full-length Rad50 lysis buffer plus 10 mM β-mercaptoethanol. Cleaved full-length Rad50 was purified as the flow through from the HisTrap column in the dialysis buffer. The sample was diluted with 50 mM Tris-HCl, 10% glycerol, 1 mM EDTA, 1 mM DTT, pH 8 to decrease the potassium chloride concentration to 75 mM and the protein sample was further purified on a HiTrap Q column in a linear gradient into 50 mM Tris-HCl, 1 M NaCl, 10% glycerol, 1 mM EDTA, 1 mM DTT, pH 8. The sample was concentrated in a 30 kDa MWCO centrifugal concentrator (Sartorius) and loaded onto a HiLoad 16/60 Superdex 200 pg column (Cytiva) equilibrated in 25 mM Tris-HCl, 100 mM NaCl, 10% glycerol, 1 mM TCEP, pH 8.

Mre11$_2$-Rad50$_2$ (MR) and Mre11$_2$-Rad50$^{NBD}{}_2$ (MR^{NBD}) complexes were made by mixing equimolar ratios of Mre11 and Rad50 or Rad50^{NBD}, heating at 60 °C for 15 min, and cooling to room temperature. For NMR, ILVM-labeled MR^{NBD} complexes were further purified over a HiLoad 16/60 Superdex 200 pg column (Cytiva) equilibrated in 25 mM HEPES, 200 mM sodium acetate, 0.1 mM EDTA, pH 7.0. NMR samples were then buffer exchanged into 25 mM HEPES, 100 mM NaCl, 1% glycerol, 1 mM TCEP, 5 mM $MgCl_2$, 0.1 mM EDTA, pH 6.60 (uncorrected) in 99% D_2O. Typically, NMR samples were 40 – 100 μM MR^{NBD} in 300 or 500 μL.

Modification of phosphorothioate DNA with the spin-label

Nitroxide-labeled DNA samples were made using commercially synthesized phosphorothioate oligonucleotides and 2-(3-iodoacetamidomethyl)-PROXYL (IAM-PROXYL; Toronto Research Chemicals). Hairpin DNA (5′-CACGCACGTAGAAGCTTTTGCTTCTACGTGCGTGAC-3′; MilliporeSigma or IDT) with a phosphorothioate incorporated at single, specific nucleotides were used without further purification. The DNAs were solubilized to 1 mM in water. TEAA was prepared by mixing equimolar quantities of triethylamine and acetic acid in water to achieve a final concentration of 0.1 M; the pH was adjusted to 6.5 using either acetic acid or triethylamine. IAM-PROXYL was solubilized in DMF to give a 10 mM solution. Equal volumes of 0.1 M TEAA (pH 6.5), 10 mM IAM-PROXYL in DMF, and 1 mM DNA were mixed in microcentrifuge tubes and incubated at 50 °C for 8 h, as previously reported[52]. After this time, the solution was dried in a speed vac and the DNA was buffer exchanged via repeated centrifugal concentration (VivaSpin, Sartorius) into 25 mM HEPES, 100 mM NaCl, 1% glycerol, 1 mM TCEP, 5 mM $MgCl_2$, 0.1 mM EDTA, pH 6.60 (uncorrected) in 99% D_2O. Labeling efficiency was determined using MALDI mass spectrometry at the Center for Metabolomics and Proteomics at the University of Minnesota. Before adding to the NMR samples, the PROXYL-labeled DNAs were heat-denatured and snap-cooled on ice to form a hairpin.

Methyl CSP and PRE analyses

All NMR experiments were performed at 50 °C on a 600 MHz (14.1 T) Agilent DD2 or 900 MHz (21.2 T) Bruker Avance III NMR spectrometer equipped with room temperature z-axis gradient HCN or cryogenically cooled z-axis gradient TCI probes, respectively. CSPs and PREs were obtained from 2D ^{13}C,^{1}H methyl-TROSY[63] HMQC experiments collected with 1148 and 144 complex points and sweep widths of 9009 Hz and 3050 Hz in the ^{1}H and ^{13}C dimensions, respectively (600 MHz data) or with 1844 and 144 complex points and sweep widths of 14423 Hz and 4500 Hz in the ^{1}H and ^{13}C dimensions, respectively (900 MHz data). Data sets were processed and analyzed with NMRPipe[64] and CCPN analysis[65] using NMRBox[66]. Side-chain methyl group assignments for apo Mre11 nuclease and capping domain (BMRB ID: 28054) and Rad50^{NBD} (BMRB ID: 27955) have been previously determined[42,49]. ILVM assignments of the DNA-bound MR^{NBD} complex were obtained by transferring the apo assignments onto the DNA-bound spectra using titration experiments. Briefly, 0.2, 0.4, 0.6, 0.8, 1.0, 2.0, and 4.0 molar equivalents of hairpin DNA were added to ILVM-labeled complexes (46.1 μM ILVM-labeled Mre11/Rad50^{NBD} and 85.6 μM Mre11/ILVM-labeled Rad50^{NBD}), and 2D methyl-TROSY HMQC spectra were recorded. Chemical shift trajectories were monitored and quantified using CCPN analysis. Binding affinities were calculated according to:

$$\Delta\delta = \Delta\delta_{max}/2\left(1 + K_D/\left[MR^{NBD}\right] + [dsDNA]/\left[MR^{NBD}\right] - \sqrt{\left(1 + K_D/\left[MR^{NBD}\right] + [dsDNA]/\left[MR^{NBD}\right]\right)^2 - 4\left([dsDNA]/\left[MR^{NBD}\right]\right)}\right)$$

where $\Delta\delta$, the shift difference, is the weighted change in chemical shift upon each addition of dsDNA (i.e., $\Delta\delta = |\delta_i - \delta_{apo}|$, where δ_i and δ_{apo} are the weighted chemical shifts for the ith addition of dsDNA and the initial apo state, respectively) and $\Delta\delta_{max}$ is the maximum change in the chemical shift[67]. For Figs. 1B and 2B, we have plotted the $\log_{10}(K_D)$ where the K_D has units of M.

Additionally, a weighted chemical shift perturbation (CSP) was calculated from the ^{1}H (δ^H) and ^{13}C (δ^C) chemical shifts according to:

$$CSP = \sqrt{\left(\frac{\delta_i^H - \delta_j^H}{w_H}\right)^2 + \left(\frac{\delta_i^C - \delta_j^C}{w_C}\right)^2}$$

where δ_i is the chemical shift value for DNA-free MR^{NBD} complex, δ_j is the chemical shift value for DNA-bound MR^{NBD} complex (4-fold molar excess),

and w_H and w_C are the standard deviations for methyl group specific δ^H and δ^C from the Biological Magnetic Resonance Data Bank (https://bmrb.io). CSP values greater than 1-times the standard deviation above the trimmed mean, which was calculated by iteratively removing CSP values greater than 2-times the standard deviation above the mean until the standard deviation was unchanged, were considered significant.

In addition to hairpin DNA, a 50-base pair dsDNA substrate (5'-CTGCAGGGTTTTTGTTCCAGTCTGTAGCACTGTGTAAGACAG GCCAGATG-3' annealed to 5'-CATCTGGCCTGTCTTACACAGTGCT ACAGACTGGAACAAAAACCCTGCAG-3' in a 1:1 ratio; IDT) was also added to the ILVM-labeled MR^{NBD} complex.

To define distance restraints between the ILVM-labeled MR^{NBD} complexes and DNA, 2D ^{13}C,^{1}H methyl-TROSY[63] HMQC experiments were collected on 1:4 ratio of MR^{NBD} complex-to-DNA without (diamagnetic) and with the PROXYL spin label (paramagnetic) at different sites within the hairpin DNA. PREs were determined from the intensities of the methyl resonances (I_{para} and I_{dia}) as previously described by Battiste and Wagner[51]:

$$\frac{I_{para}}{I_{dia}} = \frac{R_2 \exp(-PRE\, t)}{R_2 + PRE}$$

where R_2 is the ^{1}H transverse relaxation rate in the diamagnetic state and t is 7.08 ms. The diamagnetic R_2 values were estimated from the linewidth of the peak in the diamagnetic HMQC spectrum (i.e., $R_2 = \pi * \text{linewidth}$). Because of the large number of samples (twelve), with different concentrations, collected over time, intensity ratios were normalized to an isolated peak that should not have an effect due to the spin label: Val776Cγ2 (17S and 24S) or Leu44Cδ1 (2S and 36S) for $Rad50^{NBD}$ and Leu200Cδ1 (2S, 6S, and 24S) or Val41Cγ1 (17S, 30S, and 36S) for Mre11. Residues with normalized intensity ratios of less than 0.45 (17S and 24S) or 0.66 (2S and 36S) for $Rad50^{NBD}$ and 0.4 (17S) or 0.6 for Mre11 (2S, 24S, 30S, and 36S) were used in docking calculations. The distance (r) between the paramagnetic center and the side-chain methyl group were calculated according to[68,69]

$$r = \left[\frac{\mu_0^2\, \gamma_H^2\, g^2\, \beta^2\, S\,(S+1)}{15(4\pi)^2 PRE}\left(4\tau_c + \frac{3\tau_c}{1+\omega_H^2\tau_c^2}\right)\right]^{1/6}$$

where μ_0 is the permeability of vacuum, γ_H is the ^{1}H gyromagnetic ratio, g is the electronic g factor, β is the Bohr magneton, S is the electron spin quantum number, τ_c is the correlation time, and ω_H is the ^{1}H Larmor frequency. For calculating distances, the approximation was made that τ_c was equal to the global correlation time of the MR^{NBD} complex (~80 ns). Because we did not model the spin label onto the structure of the hairpin dsDNA, 7.6 Å was added to the calculated PRE distance to account for the spin label, and then the distance between the DNA backbone phosphate atom and side-chain methyl group carbon was utilized in docking calculations.

Structure calculations in HADDOCK

The models of the MR^{NBD}-DNA complex were calculated using the 'Guru' and 'multi-body' interface of the HADDOCK v2.4 webserver[53–56]. The PDBs of closed (PDB-IHM: 9A9J), partially open (PDB-IHM: 9A9K), or open (PDB-IHM: 9A9L) MR^{NBD} structural models obtained from previous HADDOCK calculations[43] and two hairpin dsDNA ensembles were used as the starting structures. Because the DNA double helix can adopt different conformations, molecular dynamics were used to increase the heterogeneity of dsDNA structures. First, an initial model of the hairpin DNA was generated with 3D-NUS[70]. Then, an ensemble of 20 hairpin dsDNA structures was created from a random selection of structures that were generated during a 10 ns molecular dynamics simulation using the CHARMM27 force field in GROMACS. When HADDOCK performs the docking simulations, one of the structures from the ensemble of 20 is randomly selected for each run. Additionally, all the nucleotides of the DNA were defined as being 'fully flexible' and C2 symmetry was enforced between the two hairpin DNAs in the HADDOCK calculations.

In HADDOCK, ambiguous interaction restraints (AIRs) are defined as the surface-exposed active and passive residues in a molecule, which take part in the binding reaction. Active residues are identified as interface residues, and passive residues correspond to their solvent-accessible neighbors[71]. Active residues in the MR^{NBD} complex were defined by the solvent-exposed residues that experienced significant CSPs (i.e., greater than 1-times the standard deviation above the trimmed mean CSP) in the NMR spectra upon DNA binding (Supplementary Fig. S5). Passive residues were defined automatically by HADDOCK. All residues in the DNA were defined as active residues, because it is not known which specific base pairs contact MR^{NBD}. For the HADDOCK docking simulations, the default random exclusion of 50% of the AIRs was used. Random removal of ambiguous restraints provides a way to deal with noisy experimental data and predictions[54]. Unambiguous restraints (i.e., distance restraints) between MR^{NBD} and the DNA were obtained from NMR PRE measurements, as described above. 66% and 33% of the PRE-based distance were used for lower and upper bounds, respectively. Such generous bounds were given because we were unsure about the effects of minor state conformations on the distance calculation from the PREs. These bounds also compensate for the unknown position of the spin label. After parsing the unambiguous restraints, the closed model based on our previously reported LRET structures had 43 restraints between each Rad50 and each DNA; the 'apo' closed MR model had 59 restraints between each Rad50 and each DNA; the partially open model had 112 restraints between each Mre11-Rad50 heterodimer and each DNA; the open model had 92 restraints between each Mre11-Rad50 heterodimer and each DNA; the closed model with the DNA loops pointed into the complex had 12 restraints between each Rad50 and each DNA; the open model with DNA loops pointed into the complex had 42 restraints between each Mre11-Rad50 heterodimer; and the closed model with one DNA had no unambiguous distance restraints (see Supplemental Information). During the rigid body energy minimization, 3000 structures were calculated, and the 200 best solutions based on the inter-molecular energy were selected for the semiflexible simulated annealing followed by explicit water refinement. Refer to the Supplementary Information for a detailed description of the rationale used for each structure calculation. Figures of the structures were made in PyMOL (Schrödinger, LLC).

To obtain a nucleotide-free, apo MR^{NBD} complex structure to use as an input in HADDOCK, previously collected LRET distance restraints[43] were used to dock two apo $Rad50^{NBD}$s (PDB ID: 3KQR)[32] to a Mre11 dimer (PDB ID: 3DSC with the DNA removed)[29]. The docking run was set up in HADDOCK as described previously for the ATP-bound MR^{NBD} complex[43]. Briefly, the number of structures for rigid body docking (it0) was increased to 3000, otherwise all settings used were default. Linkers attaching the Mre11 capping domain to the nuclease domain were allowed to be fully flexible (Y222-V236, Y249-G254, and V266-F273). C2 symmetry was enforced between the two $Rad50^{NBD}$ monomers as well as between the two monomers of the Mre11 dimer. AIRs between Mre11 and Rad50 were based on *M. jannaschii* (PDB ID: 3AV0)[36] and *E. coli* (PDB ID: 6S6V)[38] ATP-γ-S- bound MR structures. Passive AIRs were automatically defined by HADDOCK, and all AIRs were set to the default of 50% random exclusion. LRET distances[43] were input as unambiguous restraints and defined as the Cβ-Cβ distance between the LRET-labeled residues, ± 5 Å, or, for distance restraints greater than 75 Å, ±7 Å. In the crystal structure of the apo $Rad50^{NBD}$ monomer, S93 and N744 have moved significantly (7 Å and 11 Å, respectively) from their position in the AMP-PNP-bound $Rad50^{NBD}$ (PDB ID: 3QKU)[32]. Thus, LRET distance restraints utilizing these residues were omitted from the HADDOCK docking parameters. In this HADDOCK-calculated apo closed MR^{NBD} complex (PDB-IHM: 9A9M), the apo Rad50s do not form a fully closed dimer: the Walker A domain of one monomer is close to, but not interacting with, the D-loop motif of the second monomer, similar to the recently reported cryo-EM structure of ATPγS-bound *Ct* MRN[40]. Note, we also tried to generate models of partially open and open MR^{NBD} complexes using the apo Rad50 crystal structure. However, HADDOCK always returned models with Rad50s oriented in a way such that the Walker A domain and D-loop motif were pointing away from one

another - conformations, which have not been observed in any other structure of MR to date. We therefore did not use these models.

A reduced-χ^2 function ($\chi^2 = \sum_{i=1}^{n} {}^{(d_{exp,i}-d_{calc,i})^2}/d_{calc,i}/df$, where d_{exp} and d_{calc} are the experimental and back-calculated distance for each PRE (i), respectively, and df is the degrees of freedom and is equal to the number of unambiguous distances minus 6) was used to characterize the agreement between the experimental distances calculated from the PREs and the calculated distances from the HADDOCK models.

Finally, to test the robustness of the HADDOCK calculations, models for the open, partially open, and closed bound to hairpin DNA were calculated using only the PRE data (i.e., omitting the ambiguous restraints derived from the CSPs). These calculations resulted in models with all-atom root mean standard deviations of 2.76, 1.86, and 1.44 Å, respectively, from the models calculated with CPS-derived ambiguous restraints (Fig. 4), which highlights the overall robustness of the HADDOCK modeling.

LRET complex formation assay

LRET experiments were based on our previously published study[43]. A single cysteine, L51C, was introduced into wild-type Rad50^{NBD} and each of the mutant Rad50^{NBD}s (S115E/S116E, K172E, R833E/R834E, and R868E) via a modified QuikChange (Agilent) approach. The proteins were expressed and purified as described above, except a reducing agent (1 mM DTT or TCEP) was added to the purification buffers. Next, L51C-containing Rad50^{NBD}s were labeled with either Tb^{3+} chelate DTPA-cs124 EMPH (donor, LanthaScreen, Life Technologies, Inc.) or Bodipy FL maleimide (acceptor, Invitrogen) by mixing 100 µM solutions of each protein in degassed Labeling Buffer (25 mM Tris-HCl, 100 mM NaCl, 10% glycerol, 1 mM TCEP, pH 8) with a two-fold molar excess of label and incubating the reactions in the dark for 2 hr at room temperature. Unreacted label was removed via a 5 mL HiTrap Desalting column (Cytiva). For LRET measurements, 2 µM Mre11 (either full-length or nuclease and capping domain construct aa1-342) was combined with 1 µM Tb^{3+}-Rad50^{NBD} and 1 µM Bodipy-Rad50^{NBD} to make 1 µM $M_2R^{NBD}{}_2$ complex in 50 mM HEPES, 100 mM NaCl, 5 mM $MgCl_2$, 0.1 mM EDTA, 1% glycerol, and 1 mM TCEP, pH 7 buffer. Mre11 mutants were mixed with wild-type fluorophore-labeled Rad50^{NBD}s, and the fluorophore-labeled Rad50^{NBD} mutants were mixed with wild-type Mre11. 60 µL MR^{NBD} complexes were heated at 60 °C for 15 min and then split into two 30 µL reactions. 2 mM ATP was added to one of the reactions and heated at 50 °C for 10 min. After an additional 10 min incubation at room temperature, both reactions were transferred into a black, flat-bottomed 384-well plate. The plate was spun for 1 min at 500 x g before being loaded into a BioTek Synergy Neo2 plate reader (Agilent), where the samples were read for Time-resolved fluorescence (100 µsec delay, 1000 µsec data collection). Two reads were taken: ex337(20)/em490(20) for donor DPTA-Tb^{3+} fluorescence and ex337(20)/em515(20) for donor-sensitized acceptor Bodipy fluorescence. Since the Tb^{3+} emission is long-lived and the emission fluorescence is not read until after a 100 µsec delay, there was no need to correct for direct excitation of Bodipy. Thus, LRET efficiency (E) was calculated as

$$E = \frac{F}{F + D}$$

where F is the Bodipy fluorescence (due to LRET) and D is the fluorescence of the donor.

DNA binding assay

dsDNA binding to the MR complex was assayed as a change in the fluorescence polarization (FP) of a 5'-FAM (carboxyfluorescein)-labeled 40-mer dsDNA (5′-FAM-GTGTTCGGACTCTGCCTCAAGACGGTAGTCAACGTGCTT G-3' annealed to an unlabeled complementary strand; IDT) upon protein binding. Full-length MR or MR^{NBD} was titrated into 30 µL reactions containing 25 nM FAM-dsDNA substrate and 50 mM HEPES, 100 mM NaCl, 1 mM $MnCl_2$, 0.1 mM EDTA, 1% glycerol, 0.1% PEG-6000, pH 7. For dsDNA binding in the presence of ATP, closed *Pf*MR^{NBD} was formed by further heating the protein complex at 50 °C with 5 mM $MgCl_2$ and 1 mM ATP for 15 min. 5 mM $MgCl_2$ and 1 mM ATP was also included in the binding buffer. All binding reactions were incubated 15 min at room temperature and FAM FP was detected in the BioTek Synergy Neo2 plate reader using the FP 485/530 filter. FP data were fit to the Hill equation for binding:

$$FP = FP_0 + \left(FP_{max} - FP_0\right)\frac{[DNA]^n}{K_D^n + [DNA]^n}$$

where [DNA] is the concentration of DNA, K_D is the dissociation constant, n is the Hill coefficient, FP_0 is the FP in the absence of protein, and FP_{max} is FP at maximum binding.

Mre11 nuclease assays

First, Mre11 nuclease activity was assayed by monitoring the fluorescence of a 2-aminopurine (2-AP) nucleotide incorporated into a blunt-ended 29-mer dsDNA[21,29]. The dsDNA substrate was formed by annealing equimolar amounts of the two DNA strands (5′-GGCGTGCCTTGGGCGCGC(2-AP) GCGGGCGGAG-3′ and 5′-CTCCGCCCGCTGCGCGCCCAAGGCAC GCC-3′; IDT). The 2-AP cannot fluoresce until it is released from the double helix, in this case because of Mre11 nuclease activity. Each 30 µL nuclease reaction was set up in a 1.5 mL microcentrifuge tube and contained 0.5 µM MR and 1 µM 2-AP dsDNA substrate in a Reaction Buffer (50 mM HEPES, 100 mM NaCl, 5 mM $MgCl_2$, 1 mM $MnCl_2$, 1% glycerol, pH 7) with or without 1 mM ATP. Reactions were incubated at 62 °C for 30 min in a heat block, then cooled on the bench for 2 min before centrifuging at max speed for 1 min. 25 µL of each reaction was transferred into black, flat-bottom 384-well plates (Corning) and 2-AP fluorescence was quantified by a BioTek Synergy Neo2 plate reader (ex310/em375). Raw relative fluorescent units were converted into pmols of 2-AP released per min based on a free 2-AP standard curve in nuclease reaction buffer.

Mre11 nuclease activity was also assessed by denaturing PAGE. Here, the substrate was a blunt-ended 50-mer dsDNA where one strand was 5'-labeled with Alexa Fluor 647 and had five phosphorothioate linkages at the 3'-end[22] (5'-/5Alex647N/ CTGCAGGGTTTTTGTTCCAGTCTGTAGCACTGTGT AAGACAGGCCsAsGsAsTsG-3'; IDT). This was annealed to a complementary strand containing a 5'-FAM fluorophore (5'-FAM/CATCTGGC CTGTCTTACACAGTGCTACAGACTGGAACAAAAACCCTGCAG-3'; IDT). Nuclease reactions were set up as above with this substrate and allowed to proceed for 45 min at 62 °C. After incubation, 1.5 µL of each reaction was added to 28.5 µL Reaction Buffer containing 20 mM EDTA. Then 30 µL of 2X Loading Buffer (8 M urea, 20 mM EDTA, 6% Ficoll) was added. Finally, 20 µL of each sample (0.5 pmols DNA) was loaded onto 15% denaturing polyacrylamide gels. Gels were run in 1X TBE at 20 W for 3.5 hr before being imaged for Alexa Fluor 647 and FAM fluorescence on a Cytiva Typhoon 5.0.

ATP hydrolysis assay

Rad50 ATP hydrolysis assays were performed in 50 mM Tris, 80 mM NaCl, 1% glycerol, and 5 mM $MgCl_2$, pH 7.5. 60 µL reactions containing 2.5 µM MR complex and 0–300 µM ATP were incubated in 1.5 mL microcentrifuge tubes for 60 min at 62 °C, then cooled on ice. Reactions without protein at each ATP concentration (i.e., an ATP-only titration) were included for each experiment as a control for ATP degradation and PO_4 contamination. After centrifuging, 50 µL of each reaction was transferred to the wells of clear, flat-bottom 96-well plates (Greiner) and 100 µL of cold BIOMOL Green (Enzo Lifesciences) colorimetric reagent was added. The plates were centrifuged at 500 × g for 1 min and the BIOMOL reaction was allowed to proceed at room temperature for 30 min. The amount of inorganic phosphate in the sample was quantified by measuring the BIOMOL Green absorbance at 640 nm (A_{640}) in a BioTek Synergy Neo2 multi-mode reader using the path length correction function. A_{640} values were corrected by subtracting the A_{640} values of the ATP-only reactions at each ATP concentration. This corrected A_{640} was then transformed into pmols of PO_4 released/min based on a PO_4 standard curve incubated in BIOMOL Green reagent for 30 min at room temperature. Plots of pmol PO_4 released/min (v_o) versus ATP concentration

([ATP]) were fit to the Michaelis-Menten equation, including a Hill coefficient (n):

$$Vo = \frac{V_{max}[ATP]^n}{K_m^n + [ATP]^n}$$

where V_{max} is the maximum velocity and K_m is the Michaelis-Menten constant. To determine the extent to which the ATP hydrolysis reaction was stimulated by DNA, 2.7 μg of EcoRI-linearized and ethanol-precipitated pRS413 plasmid (ATCC plasmid no. 87518, New England Biolabs)[72] was included in the reaction. This corresponds to 0.029 μM DNA ends so that MR (2.5 μM) is in excess in the reaction. Note, Mre11 is inactive as a nuclease in this assay as the reaction buffer does not contain Mn^{2+}. To limit the BIOMOL Green signal to the linear part of the curve, the concentration of WT MR and mutant MR complexes that showed significant stimulation was decreased to 0.625 μM in the reaction, and the reactions were allowed to proceed for only 45 min at 62 °C. These differences were accounted for in the subsequent data transformations to obtain pmol PO_4 released/min. Fold stimulation for WT MR complex and each mutant complex was calculated by dividing the V_{max} of the reaction in the presence of DNA by the V_{max} of the reaction without DNA.

Statistics and Reproducibility

All statistical analyses for NMR and activity assay data were performed with in-house python scripts and GraphPad Prism software, version 10.4, respectively. Information regarding the curve fits used for each dataset and the number of replicates is in the respective figure legends. Data are presented as mean ± SEM (standard error of the mean) where appropriate. Replicates are defined as measurements from independent experiments. All experiments were readily reproducible.

Reporting summary

Further information on research design is available in the Nature Portfolio Reporting Summary linked to this article.

Data availability

The atomic coordinates for the apo Rad50 nucleotide-free, DNA-free MR^{NBD} (9A9M) and DNA-bound closed (9A9N), partially open (9A9O), open (9A9P), and apo (9A9Q) MR^{NBD} complexes have been deposited in the PDB-IHM. NMR data, in-house python scripts for analyzing NMR data, and PDB files of the structures can be found at https://doi.org/10.13020/kxvq-0720. Source data for NMR graphs are included as Supplementary Data S1 and Supplementary Data S2. Source data for the activity assay graphs are included as Supplementary Data S4.

Code availability

In-house python scripts for analyzing NMR data and preparing unambiguous distance restraint for HADDOCK can be found at https://doi.org/10.13020/kxvq-0720[73] or https://github.com/michaellatham77/LathamLabScripts[74].

Received: 24 September 2024; Accepted: 26 March 2025;
Published online: 02 April 2025

References

1. Cannan, W. J. & Pederson, D. S. Mechanisms and Consequences of Double-Strand DNA Break Formation in Chromatin. *J. Cell. Physiol.* **231**, 3–14 (2016).
2. Han, J. & Huang, J. DNA double-strand break repair pathway choice: the fork in the road. *Genome Instab. Dis.* **1**, 10–19 (2020).
3. Lieber, M. R. The Mechanism of Double-Strand DNA Break Repair by the Nonhomologous DNA End-Joining Pathway. *Annu. Rev. Biochem.* **79**, 181–211 (2010).
4. Cejka, P. & Symington, L. S. DNA End Resection: Mechanism and Control. *Annu. Rev. Genet.* **55**, 285–307 (2021).
5. Oh, J. & Symington, L. Role of the Mre11 Complex in Preserving Genome Integrity. *Genes* **9**, 589 (2018).
6. Paull, T. T. 20 Years of Mre11 Biology: No End in Sight. *Mol. Cell* **71**, 419–427 (2018).
7. Syed, A. & Tainer, J. A. The MRE11–RAD50–NBS1 Complex Conducts the Orchestration of Damage Signaling and Outcomes to Stress in DNA Replication and Repair. *Annu. Rev. Biochem.* **87**, 263–294 (2018).
8. Paull, T. T. & Gellert, M. The 3′ to 5′ Exonuclease Activity of Mre11 Facilitates Repair of DNA Double-Strand Breaks. *Mol. Cell* **1**, 969–979 (1998).
9. Trujillo, K. M., Yuan, S.-S. F., Lee, E. Y.-H. P. & Sung, P. Nuclease Activities in a Complex of Human Recombination and DNA Repair Factors Rad50, Mre11, and p95. *J. Biol. Chem.* **273**, 21447–21450 (1998).
10. Hoa, N. N. et al. Mre11 Is Essential for the Removal of Lethal Topoisomerase 2 Covalent Cleavage Complexes. *Mol. Cell* **64**, 580–592 (2016).
11. Aparicio, T., Baer, R., Gottesman, M. & Gautier, J. MRN, CtIP, and BRCA1 mediate repair of topoisomerase II–DNA adducts. *J. Cell Biol.* **212**, 399–408 (2016).
12. Neale, M. J., Pan, J. & Keeney, S. Endonucleolytic processing of covalent protein-linked DNA double-strand breaks. *Nature* **436**, 1053–1057 (2005).
13. Trujillo, K. M. & Sung, P. DNA Structure-specific Nuclease Activities in the Saccharomyces cerevisiae Rad50·Mre11 Complex. *J. Biol. Chem.* **276**, 35458–35464 (2001).
14. Hopfner, K.-P. et al. Structural Biology of Rad50 ATPase: ATP-Driven Conformational Control in DNA Double-Strand Break Repair and the ABC-ATPase Superfamily. *Cell* **101**, 789–800 (2000).
15. Hopfner, K.-P. et al. The Rad50 zinc-hook is a structure joining Mre11 complexes in DNA recombination and repair. *Nature* **418**, 562–566 (2002).
16. Deshpande, R. A. et al. ATP-driven Rad50 conformations regulate DNA tethering, end resection, and ATM checkpoint signaling. *EMBO J* **33**, 482–500 (2014).
17. Cassani, C. et al. The ATP-bound conformation of the Mre11–Rad50 complex is essential for Tel1/ATM activation. *Nucleic Acids Res.* **47**, 3550–3567 (2019).
18. Lee, J.-H. et al. Ataxia Telangiectasia-Mutated (ATM) Kinase Activity Is Regulated by ATP-driven Conformational Changes in the Mre11/Rad50/Nbs1 (MRN) Complex. *J. Biol. Chem.* **288**, 12840–12851 (2013).
19. Hailemariam, S., Kumar, S. & Burgers, P. M. Activation of Tel1ATM kinase requires Rad50 ATPase and long nucleosome-free DNA but no DNA ends. *J. Biol. Chem.* **294**, 10120–10130 (2019).
20. Möckel, C., Lammens, K., Schele, A. & Hopfner, K.-P. ATP driven structural changes of the bacterial Mre11:Rad50 catalytic head complex. *Nucleic Acids Res.* **40**, 914–927 (2012).
21. Herdendorf, T. J., Albrecht, D. W., Benkovic, S. J. & Nelson, S. W. Biochemical Characterization of Bacteriophage T4 Mre11-Rad50 Complex. *J. Biol. Chem.* **286**, 2382–2392 (2011).
22. Hopkins, B. B. & Paull, T. T. TheP. furiosus Mre11/Rad50 Complex Promotes 5′ Strand Resection at a DNA Double-Strand Break. *Cell* **135**, 250–260 (2008).
23. Deshpande, R. A., Lee, J.-H., Arora, S. & Paull, T. T. Nbs1 Converts the Human Mre11/Rad50 Nuclease Complex into an Endo/Exonuclease Machine Specific for Protein-DNA Adducts. *Mol. Cell* **64**, 593–606 (2016).
24. Oh, J., Al-Zain, A., Cannavo, E., Cejka, P. & Symington, L. S. Xrs2 Dependent and Independent Functions of the Mre11-Rad50 Complex. *Mol. Cell* **64**, 405–415 (2016).
25. Paull, T. T. & Gellert, M. Nbs1 potentiates ATP-driven DNA unwinding and endonuclease cleavage by the Mre11/Rad50 complex. *Genes Dev* **13**, 1276–1288 (1999).

26. Williams, R. S. et al. Nbs1 Flexibly Tethers Ctp1 and Mre11-Rad50 to Coordinate DNA Double-Strand Break Processing and Repair. *Cell* **139**, 87–99 (2009).
27. Lloyd, J. et al. A Supramodular FHA/BRCT-Repeat Architecture Mediates Nbs1 Adaptor Function in Response to DNA Damage. *Cell* **139**, 100–111 (2009).
28. Hopfner, K.-P. et al. Structural Biochemistry and Interaction Architecture of the DNA Double-Strand Break Repair Mre11 Nuclease and Rad50-ATPase. *Cell* **105**, 473–485 (2001).
29. Williams, R. S. et al. Mre11 Dimers Coordinate DNA End Bridging and Nuclease Processing in Double-Strand-Break Repair. *Cell* **135**, 97–109 (2008).
30. Sung, S. et al. DNA end recognition by the Mre11 nuclease dimer: insights into resection and repair of damaged DNA. *EMBO J* **33**, 2422–2435 (2014).
31. Park, Y. B., Chae, J., Kim, Y. C. & Cho, Y. Crystal Structure of Human Mre11: Understanding Tumorigenic Mutations. *Structure* **19**, 1591–1602 (2011).
32. Williams, G. J. et al. ABC ATPase signature helices in Rad50 link nucleotide state to Mre11 interface for DNA repair. *Nat. Struct. Mol. Biol.* **18**, 423–431 (2011).
33. Liu, Y. et al. ATP-dependent DNA binding, unwinding, and resection by the Mre11/Rad50 complex. *EMBO J* **35**, 743–758 (2016).
34. Rojowska, A. et al. Structure of the Rad50 DNA double-strand break repair protein in complex with DNA. *EMBO J* **33**, 2847–2859 (2014).
35. Seifert, F. U., Lammens, K., Stoehr, G., Kessler, B. & Hopfner, K. Structural mechanism of ATP-dependent DNA binding and DNA end bridging by eukaryotic Rad50. *EMBO J* **35**, 759–772 (2016).
36. Lim, H. S., Kim, J. S., Park, Y. B., Gwon, G. H. & Cho, Y. Crystal structure of the Mre11–Rad50–ATPγS complex: understanding the interplay between Mre11 and Rad50. *Genes Dev* **25**, 1091–1104 (2011).
37. Lammens, K. et al. The Mre11:Rad50 Structure Shows an ATP-Dependent Molecular Clamp in DNA Double-Strand Break Repair. *Cell* **145**, 54–66 (2011).
38. Käshammer, L. et al. Mechanism of DNA End Sensing and Processing by the Mre11-Rad50 Complex. *Mol. Cell* **76**, 382–394.e6 (2019).
39. Gut, F. et al. Structural mechanism of endonucleolytic processing of blocked DNA ends and hairpins by Mre11-Rad50. *Mol. Cell* **82**, 3513–3522.e6 (2022).
40. Rotheneder, M. et al. Cryo-EM structure of the Mre11-Rad50-Nbs1 complex reveals the molecular mechanism of scaffolding functions. *Mol. Cell* **83**, 167–185.e9 (2023).
41. Lafrance-Vanasse, J., Williams, G. J. & Tainer, J. A. Envisioning the dynamics and flexibility of Mre11-Rad50-Nbs1 complex to decipher its roles in DNA replication and repair. *Prog. Biophys. Mol. Biol.* **117**, 182–193 (2015).
42. Boswell, Z. K., Canny, M. D., Buschmann, T. A., Sang, J. & Latham, M. P. Adjacent mutations in the archaeal Rad50 ABC ATPase D-loop disrupt allosteric regulation of ATP hydrolysis through different mechanisms. *Nucleic Acids Res.* **48**, 2457–2472 (2020).
43. Canny, M. D. & Latham, M. P. LRET-derived HADDOCK structural models describe the conformational heterogeneity required for DNA cleavage by the Mre11-Rad50 DNA damage repair complex. *eLife* **11**, e69579 (2022).
44. Myler, L. R. et al. Single-Molecule Imaging Reveals How Mre11-Rad50-Nbs1 Initiates DNA Break Repair. *Mol. Cell* **67**, 891–898.e4 (2017).
45. Bhaskara, V. et al. Rad50 Adenylate Kinase Activity Regulates DNA Tethering by Mre11/Rad50 Complexes. *Mol. Cell* **25**, 647–661 (2007).
46. Deshpande, R. A., Lee, J.-H. & Paull, T. T. Rad50 ATPase activity is regulated by DNA ends and requires coordination of both active sites. *Nucleic Acids Res* **45**, 5255–5268 (2017).
47. Majka, J., Alford, B., Ausio, J., Finn, R. M. & McMurray, C. T. ATP Hydrolysis by RAD50 Protein Switches MRE11 Enzyme from Endonuclease to Exonuclease. *J. Biol. Chem.* **287**, 2328–2341 (2012).
48. Alderson, T. R. & Kay, L. E. NMR spectroscopy captures the essential role of dynamics in regulating biomolecular function. *Cell* **184**, 577–595 (2021).
49. Rahman, S., Beikzadeh, M., Canny, M. D., Kaur, N. & Latham, M. P. Mutation of Conserved Mre11 Residues Alter Protein Dynamics to Separate Nuclease Functions. *J. Mol. Biol.* **432**, 3289–3308 (2020).
50. Clore, G. M. & Iwahara, J. Theory, Practice, and Applications of Paramagnetic Relaxation Enhancement for the Characterization of Transient Low-Population States of Biological Macromolecules and Their Complexes. *Chem. Rev.* **109**, 4108–4139 (2009).
51. Battiste, J. L. & Wagner, G. Utilization of Site-Directed Spin Labeling and High-Resolution Heteronuclear Nuclear Magnetic Resonance for Global Fold Determination of Large Proteins with Limited Nuclear Overhauser Effect Data. *Biochemistry* **39**, 5355–5365 (2000).
52. Shepherd, N. E., Gamsjaeger, R., Vandevenne, M., Cubeddu, L. & Mackay, J. P. Site directed nitroxide spin labeling of oligonucleotides for NMR and EPR studies. *Tetrahedron* **71**, 813–819 (2015).
53. Dominguez, C., Boelens, R. & Bonvin, A. M. J. J. HADDOCK: a protein-protein docking approach based on biochemical or biophysical information. *J. Am. Chem. Soc.* **125**, 1731 (2003).
54. de Vries, S. J., van Dijk, M. & Bonvin, A. M. J. J. The HADDOCK web server for data-driven biomolecular docking. *Nat. Protoc.* **5**, 883–897 (2010).
55. van Zundert, G. C. P. et al. The HADDOCK2.2 Web Server: User-Friendly Integrative Modeling of Biomolecular Complexes. *J. Mol. Biol.* **428**, 720–725 (2016).
56. Honorato, R. V. et al. Structural Biology in the Clouds: The WeNMR-EOSC Ecosystem. *Front. Mol. Biosci.* **8**, 729513 (2021).
57. Saathoff, J.-H., Käshammer, L., Lammens, K., Byrne, R. T. & Hopfner, K.-P. The bacterial Mre11–Rad50 homolog SbcCD cleaves opposing strands of DNA by two chemically distinct nuclease reactions. *Nucleic Acids Res* **46**, 11303–11314 (2018).
58. Boswell, Z. K., Rahman, S., Canny, M. D. & Latham, M. P. A dynamic allosteric pathway underlies Rad50 ABC ATPase function in DNA repair. *Sci. Rep.* **8**, 1639 (2018).
59. Nicolas, Y. et al. Molecular insights into the activation of Mre11-Rad50 endonuclease activity by Sae2/CtIP. *Mol. Cell* **84**, 2223–2237.e4 (2024).
60. Abramson, J. et al. Accurate structure prediction of biomolecular interactions with AlphaFold 3. *Nature* **630**, 493–500 (2024).
61. Azatian, S. B., Kaur, N. & Latham, M. P. Increasing the buffering capacity of minimal media leads to higher protein yield. *J. Biomol. NMR* **73**, 11–17 (2019).
62. Tugarinov, V., Kanelis, V. & Kay, L. E. Isotope labeling strategies for the study of high-molecular-weight proteins by solution NMR spectroscopy. *Nat. Protoc.* **1**, 749–754 (2006).
63. Tugarinov, V., Hwang, P. M., Ollerenshaw, J. E. & Kay, L. E. Cross-Correlated Relaxation Enhanced 1 H− 13 C NMR Spectroscopy of Methyl Groups in Very High Molecular Weight Proteins and Protein Complexes. *J. Am. Chem. Soc.* **125**, 10420–10428 (2003).
64. Delaglio, F. et al. NMRPipe: A multidimensional spectral processing system based on UNIX pipes. *J. Biomol. NMR* **6**, 277–293 (1995).
65. Vranken, W. F. et al. The CCPN data model for NMR spectroscopy: development of a software pipeline. *Proteins* **59**, 687–696 (2005).
66. Maciejewski, M. W. et al. NMRbox: A Resource for Biomolecular NMR Computation. *Biophys. J.* **112**, 1529–1534 (2017).
67. Williamson, M. P. Using chemical shift perturbation to characterise ligand binding. *Prog. Nucl. Magn. Reson. Spectrosc.* **73**, 1–16 (2013).
68. Solomon, I. Relaxation Processes in a System of Two Spins. *Phys. Rev.* **99**, 559–565 (1955).
69. Bloembergen, N. & Morgan, L. O. Proton Relaxation Times in Paramagnetic Solutions. Effects of Electron Spin Relaxation. *J. Chem. Phys.* **34**, 842–850 (1961).
70. Patro, L. P. P., Kumar, A., Kolimi, N. & Rathinavelan, T. 3D-NuS: A Web Server for Automated Modeling and Visualization of Non-Canonical 3-Dimensional Nucleic Acid Structures. *J. Mol. Biol.* **429**, 2438–2448 (2017).

71. Dominguez, C., Boelens, R. & Bonvin, A. M. J. J. HADDOCK: A Protein−Protein Docking Approach Based on Biochemical or Biophysical Information. *J. Am. Chem. Soc.* **125**, 1731–1737 (2003).
72. Sikorski, R. S. & Hieter, P. A system of shuttle vectors and yeast host strains designed for efficient manipulation of DNA in Saccharomyces cerevisiae. *Genetics* **122**, 19–27 (1989).
73. Latham, M. P. HADDOCK Ambiguous restraint generation from NMR peak intensities. https://doi.org/10.13020/kxvq-0720 (2025).
74. Latham, M. P. HADDOCK Ambiguous restraint generation from NMR peak intensities. https://github.com/michaellatham77/LathamLabScripts (2025).

Acknowledgements

This work is supported by the National Institute of General Medical Sciences (R35GM128906). This study made use of NMRbox: National Center for Biomolecular NMR Data Processing and Analysis, a Biomedical Technology Research Resource (BTRR), which is supported by NIH grant P41GM111135 (NIGMS). For HADDOCK calculations, the FP7 WeNMR (project# 261572), H2020 West-Life (project# 675858), the EOSC-hub (project# 777536) and the EGI-ACE (project# 101017567) European e-Infrastructure projects are acknowledged for the use of their web portals, which make use of the EGI infrastructure with the dedicated support of CESNET-MCC, INFN-LNL-2, NCG-INGRID-PT, TW-NCHC, CESGA, IFCA-LCG2, UA-BITP, TR-FC1-ULAKBIM, CSTCLOUD-EGI, IN2P3-CPPM, CIRMMP, SURFsara and NIKHEF, and the additional support of the national GRID Initiatives of Belgium, France, Italy, Germany, the Netherlands, Poland, Portugal, Spain, UK, Taiwan and the US Open Science Grid. We would like to thank Monica Sekharan and Brinda Vallat at RCSB for their invaluable assistance in depositing our models into the PDB-IHM. We also thank the other members of the Latham group for helpful discussions.

Author contributions

Conceptualization, M.P.L.; Methodology, M.D.C., M.B., N.K., and M.P.L; Formal Analysis, M.D.C., M.B., N.K., and M.P.L.; Investigation, M.D.C., M.B., N.K., and R.P.; Writing - Original Draft, M.D.C., M.B., and M.P.L.; Writing - Review & Editing, M.D.C., M.B., N.K., R.P., and M.P.L.; Visualization, M.D.C. and M.P.L; Supervision, M.D.C. and M.P.L; Project Administration, M.P.L.; and Funding Acquisition, M.P.L.

Competing interests

The authors declare no competing interests.

Additional information

Supplementary information The online version contains supplementary material available at https://doi.org/10.1038/s42003-025-08003-0.

Correspondence and requests for materials should be addressed to Michael P. Latham.

Peer review information *Communications Biology* thanks the anonymous reviewers for their contribution to the peer review of this work. Primary Handling Editors: Laura Rodriguez Perez.